Hybrid perovskites for indoor photovoltaic applications
[Redacted version]

Shaoyang Wang

A thesis submitted for the degree of PhD
at the
University of St Andrews

2024

Full metadata for this thesis is available in
St Andrews Research Repository
at:
https://research-repository.st-andrews.ac.uk/

Identifier to use to cite or link to this thesis:

DOI: https://doi.org/10.17630/sta/1089

Abstract

This thesis focuses on developing efficient indoor perovskite photovoltaic device in terms of device architecture, perovskite active layer, and charge transport layers. Indoor photovoltaics are receiving tremendous attention due to the continuous development of the Internet of Things. This thesis investigates the device performance and optoelectronic properties of perovskite thin films and corresponding devices with assist of various characterisations.

The device performances are highly dependent on the architecture of devices due to different types of transport layers. How the selection of hole extraction layers (HELs) impacts the device performance is studied. For n-i-p device, The Spiro-OMeTAD-based devices show a consistently higher power conversion efficiency with fewer trap states and higher carrier lifetime compared to P3HT. For p-i-n devices, We found that the metal oxide HEL (NiO and CuO_x) based devices suffer severe light soaking effects and the bulk vs interface traps contribution to the detrimental light soaking effects. Interface modification of metal oxide transport layers using 2PACz eliminated the light-soaking effects, passivated the defects, suppressed the leakage current.

The thesis reports how the fast processing of the triple halide perovskite enables the retention of chlorine and the beneficial role of chlorine in enhancing the indoor light harvesting of a wide bandgap triple anion (TA) perovskite $CH_3NH_3PbI_{2.6}Br_{0.2}Cl_{0.2}$. The best-performing TA perovskite indoor-photovoltaic device achieved a steady-state power conversion efficiency (PCE) of 25.1% with an output power density of ~75 µW cm^{-2} under 1000 lux indoor illumination (0.3 mW cm^{-2}). Improved crystalline quality, reduced defect density and longer carrier lifetime were achieved.

Efforts are taken to realise the vision of IoT. This thesis successfully achieved photovoltaic sensor powering by direction connection, real-time monitoring, and independent power management. The results from the thesis demonstrate novel routes to develop efficient and reliable indoor photovoltaics and the potential to integrate the device with microelectronic sensors.

List of Publications

Arising from this work

- Shaoyang Wang, Paul. R. Edwards, Maged Abdelsamie, Peter Brown, David Webster, Arvydas Ruseckas, Gopika Rajan, Ana I. S. Neves, Robert W. Martin, Carolin M. Sutter-Fella, Graham A. Turnbull, Ifor D. W. Samuel, and Lethy Krishnan Jagadamma. (2023). *Chlorine retention enables the indoor light harvesting of triple halide wide bandgap perovskites*, J. Mater. Chem. A, 2023, 11, 12328. doi: 10.1039/d3ta01784b
- Shaoyang Wang, Byeong-Cheol Kang, Sang-Joon Park, Tae-Jun Ha, and Lethy Krishnan Jagadamma, *P3HT vs Spiro-OMeTAD as a hole transport layer for halide perovskite indoor photovoltaics and self-powering of motion sensors*, JPhys Mater., vol. 6, no. 2, 2023, doi: 10.1088/2515-7639/accaaa.
- Alasdair Bulloch, Shaoyang Wang, Paheli Ghosh, Lethy Krishnan Jagadamma. (2022). *Hysteresis in Hybrid Perovskite Indoor Photovoltaics.* Philosophical Transactions of the Royal Society A. 2022, 380. doi: https://doi.org/10.1098/rsta.2021.0144.
- Lethy Krishnan Jagadamma, Shaoyang Wang. (2021). *Wide-Bandgap Halide Perovskite for Indoor Photovoltaics.* Front. Chem. 9:632021. doi: 10.3389/fchem.2021.632021
- Shaoyang Wang, Tim Kodalle, Carolin M. Sutter-Fella, Sam Miller and Lethy Krishnan Jagadamma. *Metal oxide vs Organic semiconductor charge extraction layers for halide perovskite indoor photovoltaics.* Submitted to Advanced Functional Materials and under review (2024)

Outside of this thesis

- Sami Toikkonen, G. Krishnamurthy Grandhi, Shaoyang Wang, Bora Baydin, Basheer Al-Anesi, L. Krishnan Jagadamma, Paola Vivo, *Is doping of Spiro-OMeTAD a requirement for efficient and stable perovskite indoor photovoltaics?* Accepted by Advanced Devices & Instrumentation (2024)
- Lin-Jie Yang, Wenye Xuan, Sara Henda, Shaoyang Wang, Sai Kiran Rajendran, David B. Cordes, David N. Miller1, Alexandra M. Z. Slawin, Lethy Krishnan Jagadamma, Hamid Ohadi, Hsin-Yi Tiffany Chen, Matthew S. Dyer and Julia L. Payne. *Probing Intercalation in Hybrid Perovksites Using a Combined Experimental and Computational Approach.* Submitted to Nature Communication (2024)
- Graeme Cooke, Shaoyang Wang, Lethy Krishnan Jagadamma. *A BODIPY small molecule as hole transporting materials for efficient perovskite solar cells.* In preparation (2024)

Candidate's declaration

I, Shaoyang Wang, do hereby certify that this thesis, submitted for the degree of PhD, which is approximately 40,000 words in length, has been written by me, and that it is the record of work carried out by me, or principally by myself in collaboration with others as acknowledged, and that it has not been submitted in any previous application for any degree. I confirm that any appendices included in my thesis contain only material permitted by the 'Assessment of Postgraduate Research Students' policy.

I was admitted as a research student at the University of St Andrews in November 2020.

I received funding from an organisation or institution and have acknowledged the funder(s) in the full text of my thesis.

02/05/2024

Date   Signature of candidate

Supervisor's declaration

I hereby certify that the candidate has fulfilled the conditions of the Resolution and Regulations appropriate for the degree of PhD in the University of St Andrews and that the candidate is qualified to submit this thesis in application for that degree. I confirm that any appendices included in the thesis contain only material permitted by the 'Assessment of Postgraduate Research Students' policy.

02/05/2024

Date   Signature of supervisor

Permission for publication

In submitting this thesis to the University of St Andrews we understand that we are giving permission for it to be made available for use in accordance with the regulations of the University Library for the time being in force, subject to any copyright vested in the work not being affected thereby. We also understand, unless exempt by an award of an embargo as requested below, that the title and the abstract will be published, and that a copy of the work may be made and supplied to any bona fide library or research worker, that this thesis will be electronically accessible for personal or research use and that the library has the right to migrate this thesis into new electronic forms as required to ensure continued access to the thesis.

I, Shaoyang Wang, have obtained, or am in the process of obtaining, third-party copyright permissions that are required or have requested the appropriate embargo below.

The following is an agreed request by candidate and supervisor regarding the publication of this thesis:

Printed copy

No embargo on print copy.

Electronic copy

Embargo on part (Chapter 3-Chapter 6) of electronic copy for a period of 3 years on the following ground(s):

- Publication would preclude future publication

Supporting statement for electronic embargo request

The research is relatively new and experimental details for chapter 3 and 5 should be embargoed. Chapter 6 preclude further publications.

Title and Abstract

- I agree to the title and abstract being published.

02/05/2024

Date   Signature of candidate

02/05/2024

Date   Signature of supervisor

Underpinning Research Data or Digital Outputs

Candidate's declaration

I, Shaoyang Wang, understand that by declaring that I have original research data or digital outputs, I should make every effort in meeting the University's and research funders' requirements on the deposit and sharing of research data or research digital outputs.

 02/05/2024

Date   Signature of candidate

Permission for publication of underpinning research data or digital outputs

We understand that for any original research data or digital outputs which are deposited, we are giving permission for them to be made available for use in accordance with the requirements of the University and research funders, for the time being in force.

We also understand that the title and the description will be published, and that the underpinning research data or digital outputs will be electronically accessible for use in accordance with the license specified at the point of deposit, unless exempt by award of an embargo as requested below.

The following is an agreed request by candidate and supervisor regarding the publication of underpinning research data or digital outputs:

Embargo on part (Chapter 3-Chapter 6) of electronic files for a period of 3 years on the following ground(s):

- Publication would preclude future publication

Supporting statement for embargo request

Results from Chapter 3-6 are new. Chapter 6 precludes further publications.

 02/05/2024

Date   Signature of candidate

02/05/2024

Date   Signature of supervisor

Acknowledgement

It is such a wonderful journey. Started from a winter when I felt quite nervous, and now comes to the spring of beautiful St Andrews. There are so many people I would like to thank during this journey.

I would like to first offer my greatest thanks to my supervisor, Dr. Lethy Krishnan Jagadamma, for guiding me both in my research and in my life. Lethy has helped me so much from basic physical science to experimental skills and advanced concepts. She also gave me so many opportunities in presenting myself in conferences, publishing our works and finding collaborations. Besides these, Lethy is so considerate to help me when I felt anxious and confused. Whenever I need, Lethy is always there.

My sincere thanks to St Leonards College, Quantum Materials CDT and School of Physics and Astronomy from the University of St Andrews for funding me to complete this research. I also would like to thank the all the staff members that helped me in the School of Physics and Astronomy: Callum, Graham, Lesley, Dimali...my apologies that I cannot list all of them here. They are so kind and considerate. Every time I am in the department, I feel like home. My special thanks to Professor Graham Turnbull, I have enjoyed our communication so much.

I would like to thank all the members in the Energy Harvesting Research Group, especially my particular thanks to Dr. Nirmal Prashanth and Dr. Paheli Ghosh. They provided great support in my research and encouragement in my life.

I would like to thank all my dearest friends in St Andrews, Ziheng Guo, Jiawei You, Jiangmei Liu, Zhongliang Guo and Weiye Li. I enjoyed our time together so much and you always help me out whenever what happens. These are the most precious memories in my life.

Most importantly, to my parents, thank you for your endless love and support, thank you for always standing with me and understanding me.

To myself, please always remember to be kind, sincere, curious and brave.

Research data underpinning this thesis are available
at https://doi.org/10.17630/f4e1e713-4c1e-4f0f-a202-031c94f3048c。

Content

Chapter 1

Introduction

1.1. Background

The recent years have witnessed the drastic increase in demand for renewable energy. More than 500 gigawatts (GW) of renewables generation capacity is set to be added in 2024[1]. With the vision of achieving net-zero carbon dioxide equivalent emissions in the foreseen future pledged across the world, developing low-carbon electricity becomes a crucial challenge raised to the modern society. Solar photovoltaic (PV), or solar cell technology, is receiving rejuvenated attention as the most promising form of renewable energy for the harvesting abundancy and low cost[1]. Solar photovoltaic energy conversion is a one-step process generating electric energy from light energy[2]. Silicon solar cells have been developed extensively over the past few decades with high power conversion efficiency (PCE) (26.1%), and substantial reduction in manufacturing costs (0.06-0.08 USD/kWh)[3], in which case silicon solar

cells are dominating the current PV market[4]. Considering the low specific power (power to weight ratio) and rigid nature of silicon panels, thin film photovoltaic technology including, cadmium telluride (CdTe), gallium arsenide (GaAs) and amorphous silicon (α-Si:H) have been developed, which are called second-generation photovoltaics[5]. The second-generation photovoltaics provide a commercial alternative to silicon solar cells by providing better energy yield and adaption to domestic spaces due to higher optical absorption coefficient[6]. However, a critical challenge of this family of photovoltaics is the limited availability of raw material for terawatt-scale production (e.g., Te and Ga), which hinders their further application[7]. In this case, third generation solution-based thin-film solar cells including organic solar cells (OSC), dye-sensitized solar cells (DSSC) and perovskite solar cells (PSC) come into sight as emerging alternatives in research field and industry. Among them, organic-inorganic lead halide perovskite material is considered as the most promising material as a ground breaker for PV industry due to various outstanding optoelectronic properties including high absorption coefficient, long carrier diffusion length[8], defect tolerance[9] and tuneable bandgap[10]. These promising properties have triggered extensive research of perovskite solar cells and resulted in rapid development. Perovskites are a type of semiconductor generally have a crystal structure with the chemical formula ABX_3, which is consisting of A-site organic or inorganic monovalent cations (e.g. methylammonium cation, or cesium (Cs)), B-site divalent metal cation for (Pb^{2+}; Sn^{2+}; Ge^{2+}) and X-site halide anion (Cl^-; Br^-; I^-) as shown in **Figure 1-1 (a)**.

The PCE of PSCs has increased from 3.8% to the latest record of 26.1% within 15 years (**Figure 1-1 (b)**, extracted from NREL[11]). Perovskite solar cell was developed by Prof Tom Miyasaka by using $CH_3NH_2PbI_3$ for the first time in 2009[12]. In 2012, perovskite solar cells with PCE over 10% was developed by Nam-Gyu Park and Henry Sanith[13,14]. Perovskite solar cells then received readily development in recent years by shifting from liquid DSSC structure to solid state thin film architectures[14]. Extensive approaches have been developed in the past 15 years to improve the efficiency and stability of PSCs including compositional engineering[15], interfacial passivation[16], and novel transport layer development[17]. These efforts have made PSCs the most promising candidate for the next generation of PV technology for global renewable energy market for their low-cost, high efficiency and potential for large scale deployment. The highest efficiency of 26.1% is achieved up to 2023 by

adding alkylammonium chlorides (RACl) to FAPbI$_3$ to control the crystallinity and improve the phase stability by Seok et al [18]. PSCs can be fabricated by solution-based processes which are cheap and simple; different architectures (n-*i*-p & p-*i*-n) and functional layer options also provide enough space for PSCs to boost for higher PCE and better stability[19]. Above all, perovskite solar cell is considered as one of the most promising candidates for the next generation photovoltaics.

1.2. Development of IPV

Indoor photovoltaics (IPV) refers to the devices that convert artificial light inside the buildings to electricity. The concept of IPV was almost dormant until 2010 though it was developed in the 1970s. However, IPV made notable progress in the past 5 years due to the emergence of the Internet of Things (IoT)[20]. The number of publications in the IPV field has boosted rapidly since 2010 as shown in **Figure 1-1 (c)**. Internet of Things (IoT) is the ecosystem that arranges large networks to collect and communicate Big Data to monitor and optimize works in various fields[21]. Normal IoT microelectronic devices include various types of actuators or communication devices such as wireless sensors (**Figure 1-1 (d)**), Bluetooth beacons and electronic tags[22]. Currently, billions of sensor nodes are going to be built and connected to realise the vision of IoT ecosystems including smart and secured building and vehicles. It is estimated that 30 billion IoT components will be installed by 2025[23]. Furthermore, it is noticeable that half of those components to be installed will locate inside buildings. Figure 1-1 (c) exhibits general components of a microelectronic IoT devices and wireless sensors are one of the most fundamental elements. At present, these wireless sensors are powered by batteries and this limits the size and wide applicability of IoT. Sustainably powering of these IoT sensors becomes a critical and serious issue since traditional batteries or grid-connected electricity are not suitable for large scale deployment of IoT components. On the one hand, traditional batteries require frequent replacement and maintenance hence the cost will become higher, these additional operations could also cause interruption to the system which will limit the application of IoT. On the other hand, the consumption of a large number of batteries will cause environmental issues as they have a limited life span[24]. In this case, alternative energy

supply technologies which are low-cost, easy-deployable, environmental-friendly, and suitable for indoor application are needed to be applied. Since light energy is abundant inside the buildings and can be easily captured and converted by photovoltaic devices, IPV becomes a promising candidate and has been emerged in recent years[25]. In addition, the power requirement of IoT components continuously decreased in recent years, IoT sensors now only need micro-to milli watt range of power to operate, which is another important reason for the emergence of IPV because this range of power can be achieved by photovoltaic cells [20].
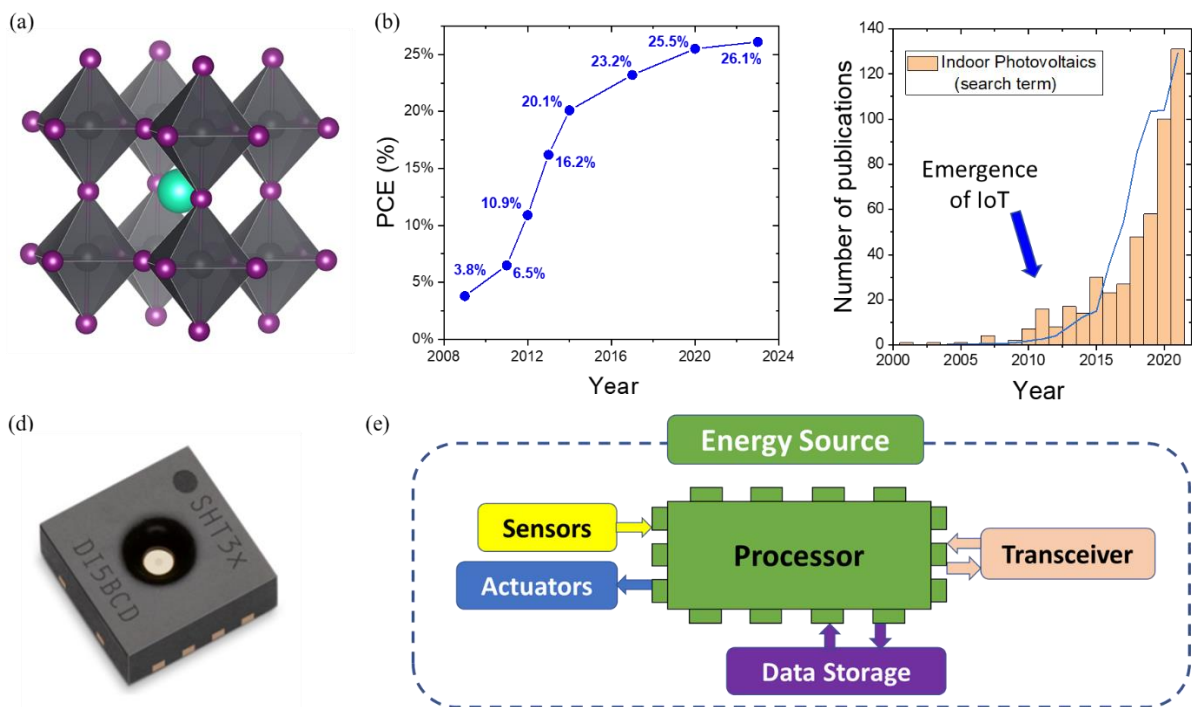
Figure. 1-1 (a) Presentation of metal halide perovskite structure. (b) PCE progress of perovskite solar cells. Figure reproduced from NREL chart. (c) The number of IoT publications in recent years. (d) Typical image of IoT microelectronic temperature and humidity sensor. (c) General components of microelectronic IoT devices.

1.3. Light illumination difference of Indoor Light and Sunlight

To investigate indoor photovoltaic application, the difference between indoor light and sunlight needs to be identified so that photovoltaic cells can be modified to fit for indoor

application. Indoor light, also known as dim-light, ambient light or artificial light, is dominated by the fluorescent lamp and white light-emitting diodes (LED) located inside the buildings. LED is a semiconductor device that emits lights while applying current flow. Electrons from current flow recombine with holes and release energy as a form of photon. Fluorescent lamp glows as a result of phosphor coating inside the lamp, which is caused by the mercury vapor excitation by applying current. The difference between indoor light and sunlight can be concluded in two aspects: i) light intensity; ii) spectral content iii) spectral range[26,27].

The standard illumination level for sunlight is defined as Air Mass 1.5 (AM 1.5G) which represents the solar irradiance received yearly at mid-latitudes from the sun being at an angle of 41.8°, corresponding to 100 mW/cm^2. While for indoor light, the normal light intensity is 0.1-1 mW/cm^2. Thus, the light intensity of indoor light is 100-1000 times lower than sunlight. The dramatic low light intensity for indoor light made defect control an important topic for indoor perovskite photovoltaic investigation. Since low light intensity generates much fewer hole-electron pairs, a higher ratio of electron/hole could be trapped by defects hence photovoltaic performance will be reduced[28]. As for spectral content exhibited in **Figure. 1-2 (a)**, sunlight has a broad active illumination range from 250 to 1750 nm while indoor light spectra are much narrower. The wavelength range of indoor light illumination is limited in visible wavelength range starting from 400 nm and cut off at approximately 780 nm.

The gap of Illumination spectra indoor light and sunlight requires the semiconductor bandgap to be optimized for IPVs. The optimal bandgap to maximize the power conversion efficiency (PCE) of indoor PV for a single junction device is 1.9 eV according to the theoretical efficiencies from Shockley-Queisser theory (compared to 1.4 eV for 1 sun illumination) as shown in **Figure. 1-2 (b)**[29]. Semiconductors designed for solar application has broad absorption spectrum, but the mismatch between broad absorption spectrum and narrower indoor illumination spectrum reduces the potential to obtain high open-circuit voltage (*V*oc). **Figure. 1-2 (c)** shows the indoor fluorescent spectrum and external quantum efficiency (EQE) spectrum of MAPbI$_3$, which is the most common perovskite composition for perovskite solar cells. It can be seen that the indoor light spectrum terminated at 650 nm while EQE of MAPbI$_3$ extends to 800 nm. The non-absorbing wavelength range does not contribute to photocurrent. In this case,

the optimization of the semiconductor bandgap becomes one of the most critical steps to develop indoor photovoltaics[30]. The amenability to bandgap tuning is one of the most important reasons that hybrid perovskites become the strongest candidate for indoor photovoltaics. The bandgap tunability and the corresponding band structure and compositional modification will be further discussed in Section 1.5.4.
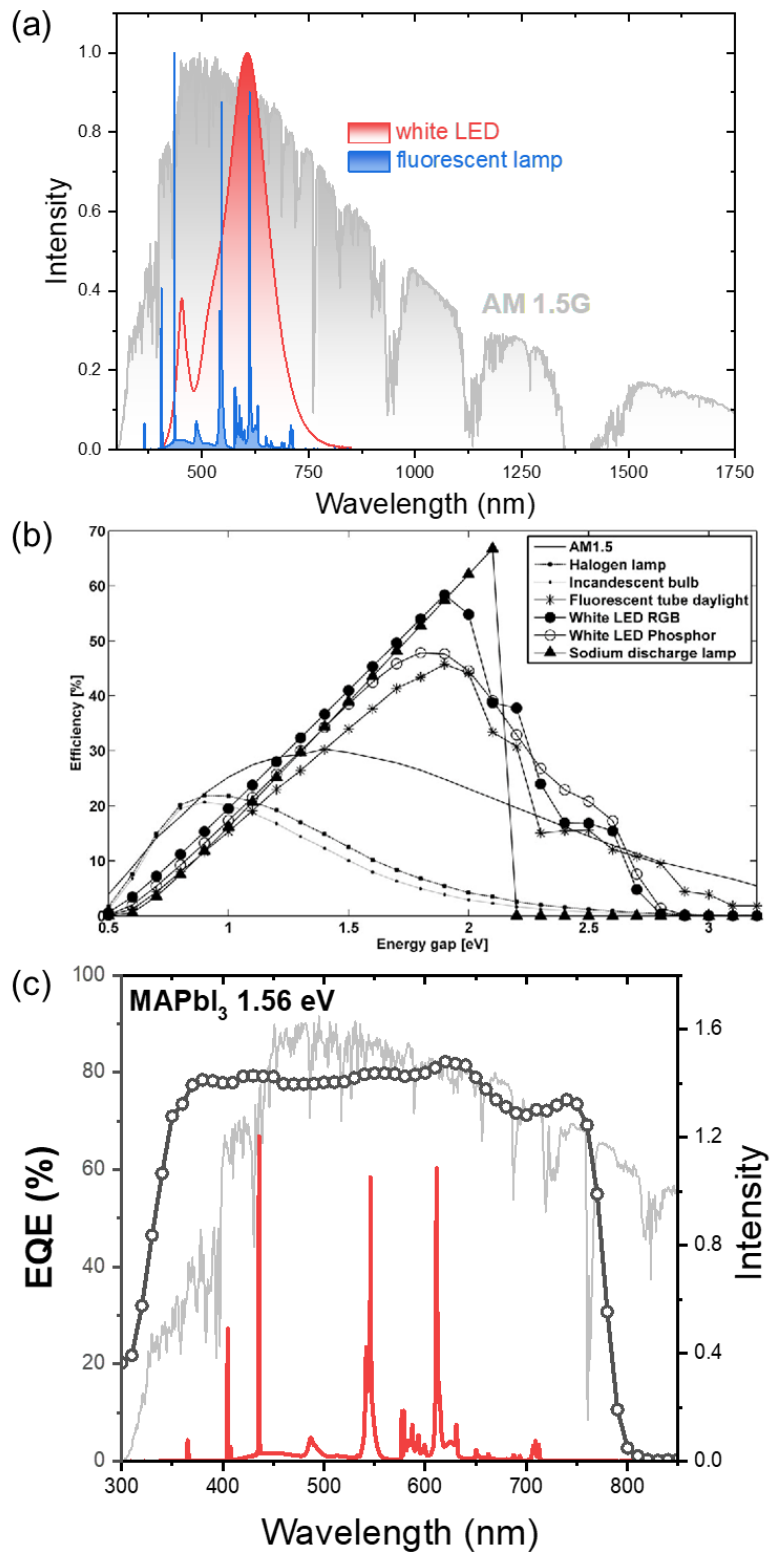
Figure. 1-2: (a) Irradiance content of AM 1.5G sunlight, white LED and fluorescent lamp. (b) Theoretical calculation of ideal PV device under different light sources. (c) MAPbI₃ EQE spectrum and indoor fluorescent spectrum.

1.4. Theoretical Parameters for Indoor Light Harvesting

1.4.1. Electronic Band Theory

Electronic band structures describe the energy that electros have and provide explanation of the electronic properties of a material. The electrons in set into different energy levels. There are also energy levels which have higher energy and not filled by electrons. When a crystal, or solid is formed, atoms gather to form clusters, the energy levels hybridise accordingly and split into several different levels. In other words, continuous band of energy levels will form as a result of close spacing of large groups energy levels due to gathering of atoms[31].

A typical energy band diagram of a semiconductor is illustrated in Figure 1-3. Fermi level (E_F), vacuum level (E_{vac}), work function, ionisation potential, bandgap, valence band and conduction band are critical parameters for electronic materials. Not only these parameters define the electronic structures and charge exchange processes of a material, it also reflects the multiplicity of internal and external factors including the purity of material, surface crystallography orientation and morphology[32].

Vacuum level Electrons are naturally bound to the solid and are prevented to escape from the surface of the material. The energy of a free and stationary electron outside the material holds is defined as vacuum level[33]. The vacuum level is defined under perfect vacuum.

Bandgap In a semiconductor, the lower energy level that the electrons are bound is defined as valence band (E_V). The energy level where the electrons are excited and free to move is defined as conduction band (E_C). The energy required to excite an electron from the ground state, which is E_V, to the excited state, which is E_V, is the bandgap of a semiconductor.

Ionisation potential is the minimum energy required to remove an electron from a neutral atom, which corresponds the energy gap between vacuum level and valence band.

Fermi level is the highest energy level that an electron could occupy at the absolute zero temperature[34]. In semiconductors, Fermi level lies between valence band and conduction band. Fermi level can be considered as a hypothetical energy level that the probability of being occupied by an electron is 50% at this energy level. The Fermi level of a semiconductor can be affected by temperature or the number of impurities. The Fermi level will shift towards conduction band if the semiconductor is doped with excess electrons and become a n-type semiconductor. A p-type semiconductor is created if the semiconductor is doped by holes and the Fermi level will shift towards valence band. Since Fermi level measures the probability of electron occupancy at different energy levels, the closer the Fermi level is to the conduction band, the easier the electrons could be excited from valence band to conduction band.

Work function is the minimum energy required to remove an electron from the surface of a solid to vacuum, it is the energy gap between the Fermi level and vacuum level[33].
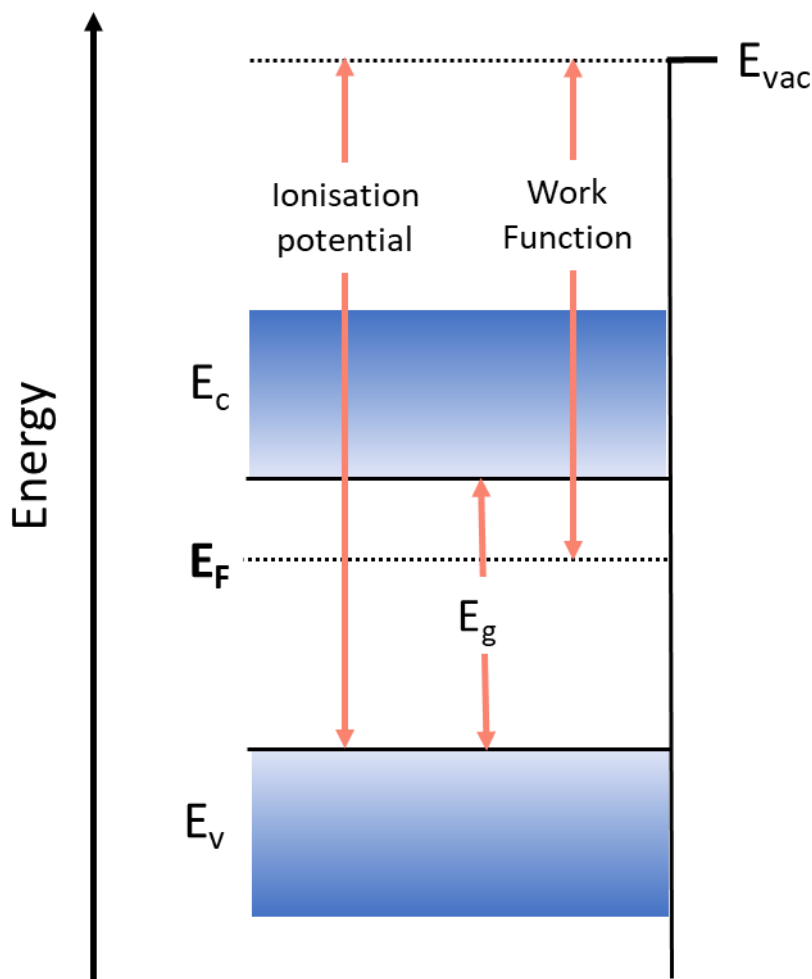
Figure. 1-3: Energy band diagram of a semiconductor, where valence band, conduction band, vacuum level, fermi level, ionisation potential and work function are defined.

1.4.2. Theory of Photovoltaic Effect and Solar Cell

Photovoltaic effect refers to the process which generates electrical energy from light energy. In a solar cell, the photovoltaic effect is consisting of 4 basic steps: the absorption of light and generation of hole-electron pairs; the separation of opposite type of charge carriers and the extraction of charge carriers to external circuits[2].

Specifically, when a photon with higher energy than the bandgap is absorbed by a semiconductor, the energy is given to an electron and excite it from conduction band (CB) to valence band (VB), leaving a hole in the valence band, thus a hole-electron pair is generated. After the photogeneration, the charge carriers need to be separated, this is usually done by p-n junction in silicon solar cells, as shown in **Figure 1-4 (a)**. p-n junction is comprised of a n-type silicon layer (boron doping for excess electrons) and a p-type silicon layer (phosphorus doping for excess holes). Since the work function of p-type semiconductor is higher than the n-type semiconductor, the electrostatic potential is smaller at the n-type semiconductor compared to p-type layer. An electric field is generated at the junction. A potential difference which is called built-in potential (V_{bi}) is generated, driving the electrons towards n-type side and holes towards p-type side. A depletion zone is generated at the interfaces where the two layers contact. Within the depletion zone, the current is formed by drifting electrons towards n-side and drifting electrons towards p-side.

For perovskite solar cells, a p-*i*-n or n-*i*-p junction is used as shown in **Figure 1-4 (b)**, which is a variation of p-n junction. It is comprised of an undoped intrinsic semiconductor, which is perovskite layer, spatially sandwiched by a p-type semiconductor and a n-type semiconductor, respectively. The same V_{bi} is achieved to generate current for solar cell operation. Specific working principles are described in Section 1.5.3.
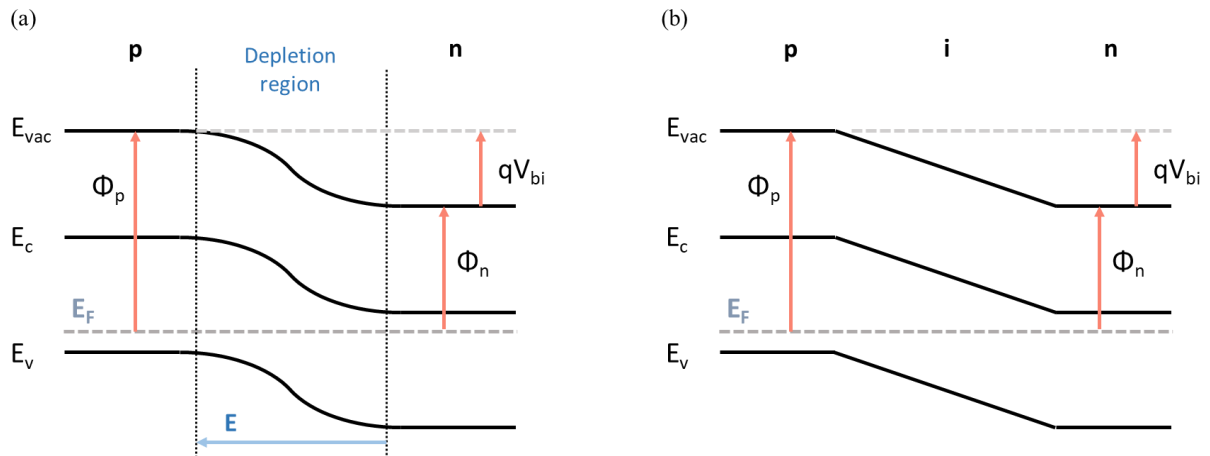
Figure. 1-4: Semiconductor junction of (a) p-n junction, (b) p-i-n junction.

1.4.3. Photovoltaic Parameters and Light Dependence

To investigate and improve the performance of indoor photovoltaics, the photovoltaic parameters which determine PCE need to be identified. The PCE of a solar cell is characterised by *J-V* measurement, where *J* refers to current density and *V* stands for voltage. A typical *J-V* curve measured from *J-V* characteristics is exhibited in **Figure. 1-5**.
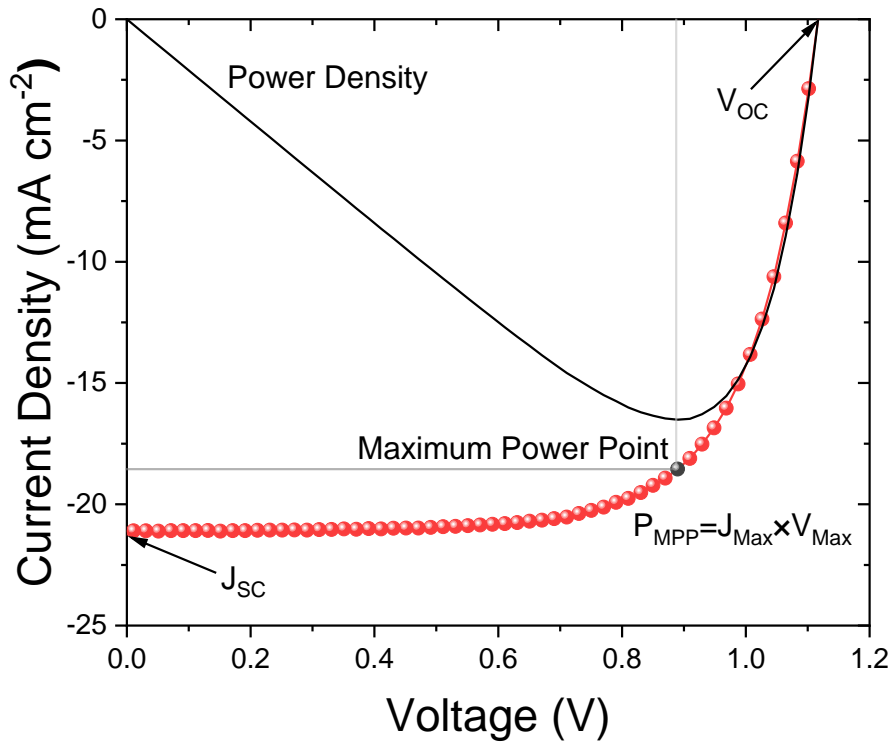
Figure. 1-5: Typical *J-V* curve of solar cell from *J-V* characteristic.

The output power density can be calculated via:

$$P = J \times V \qquad \text{(1-1)}$$

The PCE is determined as a function of incident power, which can be further clarified by three key parameters: open-circuit voltage (V_{OC}), short circuit current (J_{SC}) and fill factor (FF):

$$PCE = \frac{P_{out}}{P_{in}} = \frac{J_{sc} \times V_{oc} \times FF \times 100\%}{P_{in}} \qquad \text{(1-2)}$$

The V_{OC} indicates the point where the current flow of the cell is zero, and the output voltage of a solar cell is the maximum. The J_{SC} refers to the point where the applied voltage is zero, and the output current of a solar cell is the maximum. FF is the estimation of the ratio of maximum power of the solar cell to the product of V_{OC} and J_{SC} which can be calculated by:

$$FF = \frac{P_{out}}{J_{sc} \times V_{oc}} \qquad \text{(1-3)}$$

Photovoltaic devices can be modelled by an equivalent circuit which can be comprised of a current source, an ideal diode with its characteristic saturation current I_0 and ideality factor n, and two parasitic resistances (series resistance R_s and shunt resistance R_{sh}), as shown in **Figure 1-6 (a)**. The current source represents the photocurrent generated under illumination. Series resistance R_s takes into account the intrinsic resistance of electrodes and layers, and the connection resistance between electrodes and interlayers, which should be minimized to reduce voltage loss. Shunt resistance R_{sh} is relevant to the leakage current of the diode, it represents the loss of carriers caused by pinholes in the film and recombination happened at the interfaces hence R_{sh} should be maximized to minimise the energy losses[35,36].

In terms of the equivalent circuit, photocurrent is generated under illumination but for working conditions, the current through diode and shunt resistance should be included which can be expressed by:

$$I = I_L - I_D - I_{sh} \qquad \text{(1-4)}$$

By substituting I_D and I_{sh}, the equation of current can be obtained as below[37]:

$$I = I_L - I_0 \left[\exp\left(\frac{V+IR_S}{n_{id}V_T} \right) - 1 \right] - \frac{V+IR_S}{R_{sh}} \qquad \text{(1-5)}$$

Where n_{id} is the ideality factor which will be explained further in the next paragraphs, and V_T is the thermal voltage:

$$V_T = \frac{k_B T}{q} \qquad \text{(1-6)}$$

In terms of the equation of current I, regarding the circuit is under open circuit condition hence current is zero, with assumption that R_{sh} is far larger than R_s, a relationship between light intensity and V_{OC} can be derived by rearranging the equation[38]:

$$V_{oc} = \frac{n_{id}k_B T}{q} ln\frac{I_L}{I_0} = \frac{n_{id}k_B T}{q} lnL \qquad \text{(1-7)}$$

where k_B is Boltzmann factor, n_{id} is ideality factor, L stands for light intensity, since the change of I_L follows the light intensity variation linearly, the ratio $\frac{I_L}{I_0}$ can be considered as light intensity.

The relationship between electrical parameters and light intensity is critical for indoor photovoltaic research due to the intensity variation of indoor light and sunlight, the parameter can be directly reflected by light intensity-dependent plots and this information can be used to compare among the devices[39]. In terms of the derived V_{OC} equation, it can be seen the slope of V_{OC} versus light intensity is determined by ideality factor n_{id} which reflects the level of recombination[40]. In general, an ideality factor of 1 indicates radiative recombination, but non-radiative recombination caused by traps, which is also known as Shockley-Read-Hall (SRH) recombination is pronounced when the ideality factor closes to 2[41,42]. Since non-radiative recombination is induced by traps, the defect level within photovoltaic devices can be obtained by observing the slope of the plot of V_{OC} versus light intensity.

Regarding the relationship of J_{SC} versus light intensity, the ideal situation is that one electron-hole pair will be generated for one incident photon, in which case a recombination factor of 1 is defined[20,41].

$$I \infty I^{\alpha} \qquad (1\text{-}8)$$

In a realistic scenario, due to charge accumulation, the recombination factor α will be slightly lower than 1 so that charge transport condition can be obtained by observing the slope of the current versus light intensity plot when comparing different devices.

The fill factor (FF) is influenced by the light intensity in an indirect way whereas is closely dependent on shunt and series resistance[20,43]. Under low intensity indoor light, since the reduction of J_{SC} is more significant than V_{OC}, shunt resistance has a more significant impact on FF[44].

$$FF_{s+sh} = FF_s \left[1 - \left(\frac{v_{oc}+0.7}{v_{oc}} \right) \frac{FF_s}{r_{sh}} \right] \qquad (1\text{-}9)$$

$$FF_s = FF_0 [1 - r_s] \qquad (1\text{-}10)$$

where FF_{s+sh} is the FF including the effect of series and shunt resistance, FF_s is the FF that only considering the influence of series resistance and FF_0 stands for the ideal FF.

v_{oc} is normalized open circuit voltage, r_s and r_{sh} are normalized shunt and series resistance, respectively,

$$v_{oc} = \frac{V_{oc}}{V_T} \qquad (1\text{-}11)$$

$$r_s = \frac{R_S}{R_{CH}} \qquad (1\text{-}12)$$

$$r_{sh} = \frac{R_{sh}}{R_{CH}} \qquad (1\text{-}13)$$

and R_{CH} is the characteristic resistance given by (where A is the area of the cell)

$$R_{CH} = \frac{V_{oc}}{(J_{sc} \times A)} \qquad (1\text{-}14)$$

In conclusion, the above light-dependent parameters need to pay particular attention to understand the mechanism of indoor perovskite photovoltaics. Since all the parameters contribute to PCE, how PCE could be dependent on light intensity and spectrum also needs to be investigated. In addition, the bandgap tunability of perovskite materials makes it more important to predict the behaviour of perovskite photovoltaics both under indoor illumination and sunlight in a theoretical approach. In this case, Shockley-Queisser efficiency limit will be discussed in the next section.

1.4.4. Efficiency Limit for Indoor Photovoltaics

Shockley-Queisser (SQ) limit is the maximum theoretical efficiency limit of a single-junction photovoltaic which is dependent on the bandgap of the semiconductor[45]. SQ limit is calculated by assuming that every incident photon with higher energy than the bandgap will be absorbed and converted to an electron-hole pair while photons with lower energy than the bandgap will not be absorbed. SQ limit is computed by considering the illumination spectrum and losses from different aspects, which can be given by[46,47]:

$$\eta_{SQ} = \eta_u \times \eta_d \times \eta_{FF} \qquad (1\text{-}15)$$

where η_u is ultimate efficiency, η_d is the detailed-balance efficiency and η_{FF} is fill factor loss. These are three sources of efficiency loss, the ultimate efficiency loss is from the subgap absorption loss and the thermalization loss that high energy electron-hole pairs relaxing to band edges; detailed-balance loss due to radiative recombination that happened within solar cell black body. And fill factor loss originates from the parasitic resistance of the current-voltage characterisation[48,49]. An illustration of losses for sunlight condition is given by **Figure 1-6 (b)**.

A maximum efficiency curve for both sunlight and indoor illumination (LED and fluorescent lamp) is shown in **Figure 1-6 (c)**[46]. It can be seen that for sunlight, the maximum efficiency reached higher than 30% for an optimal bandgap between 1 and 1.5 eV. For higher bandgap, a larger amount of photons with low energy are not able to be absorbed. On the other hand, for smaller bandgaps, more photons can be absorbed but for those photons with higher energy, the thermalization loss down to the band edge becomes much more significant.

As for the SQ limit efficiency for indoor conditions, the maximum efficiency value reaches ~57% at the bandgap of 1.82~1.96 eV. Since the indoor light illumination spectrum is much narrower compared to the sunlight spectrum, overall photon energy is higher so that the optical bandgap is increased correspondingly. The non-absorption losses and thermalization loss originating from the photogenerated carrier relaxation are reduced due to the larger bandgap. These factors increase the theoretical PCE limit for IPVs than sunlight conditions[50].
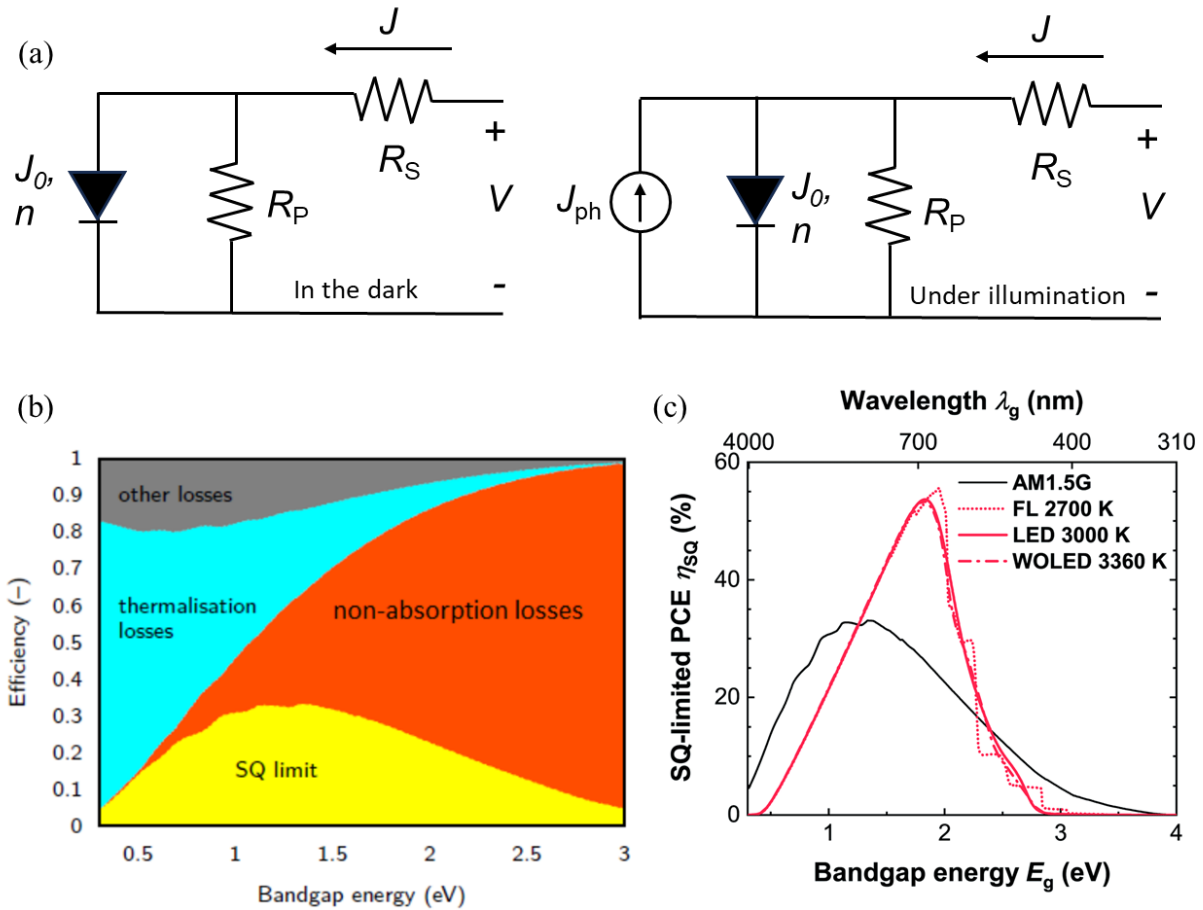
Figure 1-6: (a) Equivalent circuit of perovskite solar cells[35]; (b) illustration of theoretical losses of SQ limit model; (c) Theoretical maximum PCE for AM 1.5G solar illumination and indoor light as a function of bandgap[46].

1.5. Basic Principles of Metal Halide Perovskite Photovoltaics

1.5.1. Introduction of metal halide perovskite material

As has been previously discussed in Section 1.1, organic-inorganic lead halide perovskite materials have attracted tremendous attention in the photovoltaic field due to various outstanding optoelectronic properties including high absorption coefficient (10^5 cm^{-1})[51], long carrier diffusion length (>1000 nm)[8], defect tolerance[9] and tunable bandgap[10]. Perovskites generally have a crystal structure with the chemical formula ABX_3 (**Figure 1-7**). In this general formula, A stands for monovalent organic, e.g.

methylammonium cation, or inorganic cations, cesium (Cs), etc. B represents divalent metal cation (Pb^{2+}; Sn^{2+}; Ge^{2+}) and X represents halide anion (Cl^-; Br^-; I^-).

In a perovskite lattice structure, B cation locates in the centre of lattice cubic, surrounded by octahedral anions X, A cation maintains 12-fold cuboctahedral coordination and sit in the corners of lattice[10]. In this case, the size of A cation is crucial for perovskite lattice formation as it must be able to fit into the interspace constructed by the four surrounding octahedrons[10]. Concerning the formation of perovskite lattice, the formability of perovskite lattice could be predicted statistically by Goldschmidt's tolerance factor, $t = (r_A + r_X)/[\sqrt{2}(r_M + r_X)]$, r_A, r_M and r_X in the equation are ionic radius of A, B and X respectively, the most favourable tolerance factor for perovskite structure formation ranges from 0.8 to 0.9[30].
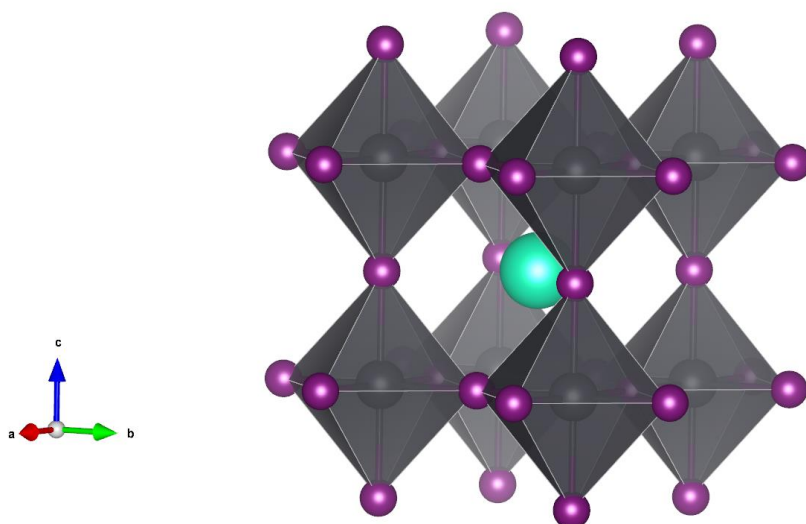
Figure 1-7: ABX$_3$ crystal structure of perovskite materials. Green molecule is A- organic or inorganic cation, B- is metal cation represented by grey molecules inside octahedron and C- (purple) is halide anion.

1.5.2. Device Architecture of Perovskite Photovoltaics

The development of perovskite solar cell is benefited from the success of DSSCs[51]. Perovskite photovoltaic devices can be fabricated by two approaches: (i) by sensitizing perovskite to mesoporous metal oxide layer, (ii) planar thin-film architecture (including n-*i*-p and p-*i*-n)[52]. For mesoporous perovskite photovoltaics, the device is comprised

of a transparent conductive oxide (FTO or ITO), a compact titania hole blocking layer, a mesoporous TiO_2 as electron transport layer (ETL), perovskite active layer, a hole transport layer (HTL, i.e. Spiro-OMeTAD), and a metal electrode.

For thin-film planar perovskite photovoltaics, the perovskite active layer is sandwiched by HTL and ETL, respectively as shown in **Figure 1-8**. The position of ETL and HTL is dependent on whether the device architecture is n-*i*-p or p-*i*-n. For n-*i*-p devices, a n-type ETL layer is deposited on the top of the transparent conductive oxide layer. Over the perovskite active layer, a p-type HTL contact is positioned. For p-*i*-n devices, the position of HTL and ETL is opposite[53]. The selection of transport layer material is an important topic for both PV research and industry since it can determine the power conversion efficiency, fabrication cost and performance stability. These charge transport layers should possess high transparency in the wavelength region used for the illumination source, good energetic alignment with the respective band edges of the perovskite active layer for charge selectivity and excellent charge transport properties. For HTL, its highest occupied molecular orbital (HOMO) should be higher to the VB of perovskite layer. For ETL, its lowest unoccupied molecular orbital (LUMO) should be lower to the CB of perovskite layer to achieve efficient charge transport as shown in **Figure. 1-8 (a)** and **(b)**. In n-*i*-p devices, the most commonly used HTL material in the halide perovskite solar cells is 2,2',7,7'-tetrakis(N,N-di-p-methoxyphenylamine)-9,9'-spirobifluorene (spiro-OMeTAD)[51]. Extraordinary performance over 25% is achieved by devices employing spiro-OMeTAD as HTL. Other promising HTL materials are PTAA [poly[bis(4-phenyl)(2,4,6-trimethyl-phenyl)amine], poly-TPD [poly(4-butylphenyldiphenylamine)] and poly(3-hexylthiophene) (P3HT)[54]. Among these, P3HT is particularly important because of its excellent optoelectronic properties, low cost, scalability and further, P3HT does not require any additional doping for efficient hole extraction[55]. Both PTAA and poly-TPD are less industry friendly due to their high cost and relatively low performance compared to Spiro-OMeTAD[56].

In the p-*i*-n perovskite solar cell devices, [6,6]-Phenyl-C61-butyric acid methyl ester (PCBM) is the most commonly used electron extraction layer for its superior energy level matching and reduced *J-V* hysteresis[51]. For extracting holes, poly (3,4-ethylenedioxythiophene)/poly (styrene sulfonic acid) (PEDOT-PSS) used to be the

most commonly employed transport layer. However, PEDOT-PSS has the issue of relatively lower efficiency due to interfacial defects and faster degradation[57]. Inorganic transport layers include Nickel oxide (NiO_x) and copper oxides (CuO_x) have also become another promising candidate for more efficient, stable and cost-effective p-*i*-n perovskite solar cells[58,59].
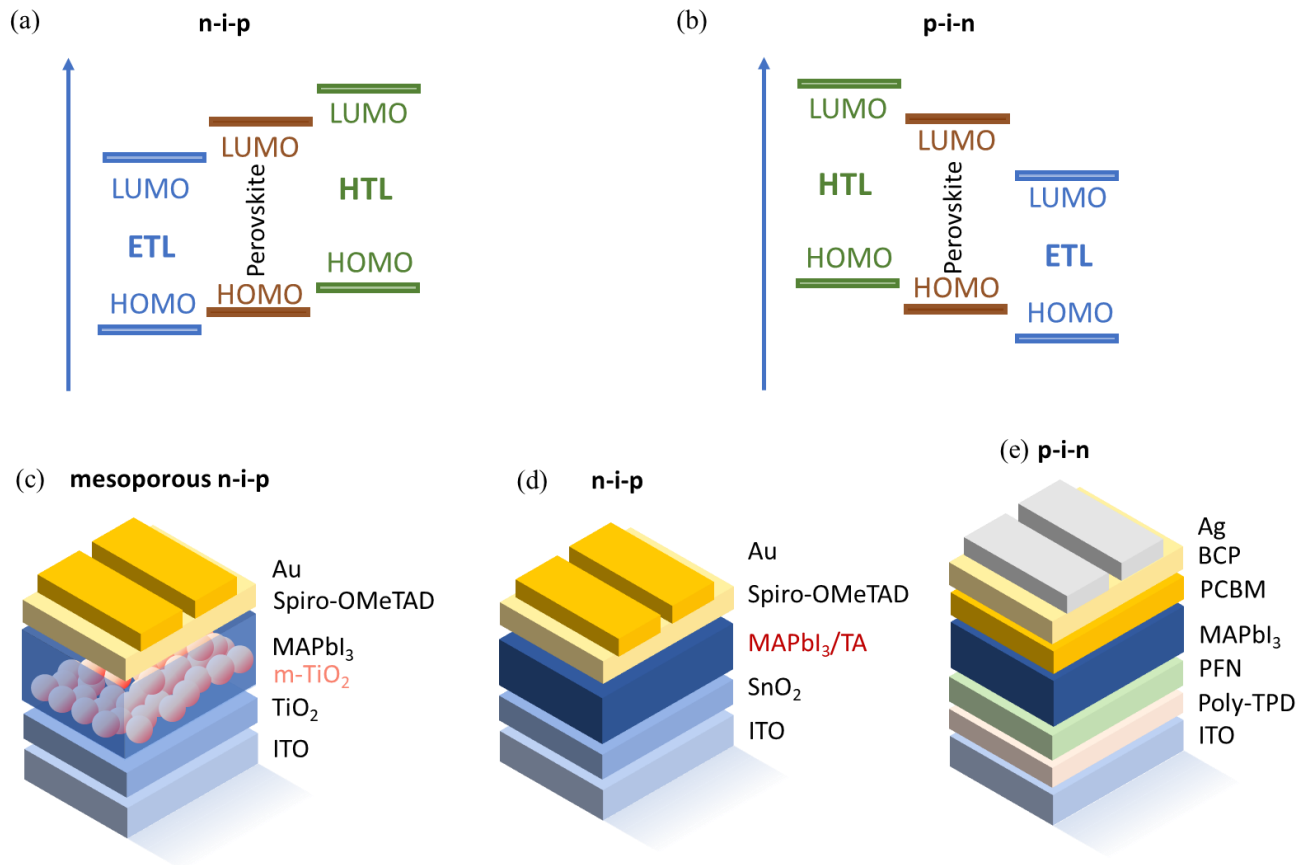
Figure 1-8: Energy diagram of typical perovskite solar cel of (a) n-*i*-p and (b) p-*i*-n junction. Three different device architecture of perovskite photovoltec cells; (b) mesoporous n-*i*-p (c) planar n-*i*-p and (d) p-*i*-n structure.

1.5.3. Working Principle of Perovskite Photovoltaics

Based on the photovoltaic parameters and device architecture discussion, the working principle of perovskite photovoltaics needs to be discussed to understand the correlation between theoretical parameters and realistic photovoltaic working process.

Since the working principle of n-*i*-p and p-*i*-n device are the same, the difference between the two is the travelling direction of charge carriers (Figure 1-8 (a) and (b)), so that p-*i*-n device will be discussed in this case as an example. The model below (**Figure 1-9 (a)**) is a typical band diagram of p-*i*-n perovskite photovoltaic cell[60].

The operation of perovskite photovoltaic cells includes four steps: light absorption, charge generation/separation, charge transport and collection to the electrodes. Light illumination could generate hole-electron pairs, electrons are excited to the conduction band and holes remain at valence band, hence produce quasi-Fermi level splitting, E_{Fn} and E_{Fp}, respectively. The gap between the two levels is the maximum available energy, which is known as open circuit voltage V_{OC}. The second step is charge separation to push the energy of quasi-Fermi level to operation[60,61].

Semiconductor needs to be contacted with charge selectivity contacts HTL and ETL, respectively. Under short-circuit conditions, fermi level is aligned so an equilibrium Fermi level E_{F0} is obtained. Since HTL and ETL have high and low work functions, respectively, a built-in potential V_{bi} is created by Fermi level equilibration, the bands of semiconductor are inclined with an electrical field, which electrons and holes will be pushed to travel through ETL and HTL[60]. For the working conditions between J_{sc} and V_{OC} points, excited electrons which diffuse to the ETL side without being consumed by the spontaneous recombination will jump to the ETL energy level from the conduction band due to potential difference, they will then be extracted from the anode and flow through an external circuit and reach the counter electrode. The same process takes place with holes at the HTL side and cathode, the holes with positive charges will jump from perovskite to the hole transport layer and reach the cathode (**Figure 1-9 (b)**). In this case, the HTL and ETL materials should be appropriately selected to achieve good quasi-fermi level splitting for better voltage and sufficient driving force V_{bi} for efficient charge transport[62].

1.5.4. Band Structure of Perovskite Material

In previous sections, it is discussed that both electronic parameters and charge collection are determined by the band structure of perovskite and charge transport layers, hence the band structure of perovskite materials needs to be investigated to

obtain better photovoltaic cells. Perovskite materials have a direct bandgap with a sharp band edge, which indicates the absorption coefficient drops sharply when close to the wavelength corresponding to the bandgap energy[63]. For low-quality materials, tail states often occur at the band edge due to the existence of defects and the band edge is gently sloping, which induced more recombination. Perovskites have a sharp band edge decay with low tail states, which suggests well ordered microstructure and enables high open-circuit voltages.

Bandgap tunability plays an important role in the development of perovskite photovoltaics, the bandgap of perovskite materials can be widened or reduced by substituting B- or X- site to obtain a broader or narrower absorption spectrum[10]. A- site is electronically inactive and does not have a direct effect on band structure, but the different size of A-site cations contributes to crystal BX_6 octahedral tilting which affects structural stability[64]. On the other hand, both conduction band and valence band are determined by s-p anti-bonding sigma orbital contributed by B cation and X anion as shown in **Figure 1-9 (c)**. The valence band is constituted by a hybrid mixture of B- site metal orbitals ns^2 and X- site halide orbitals np^6, where the major contribution is from halide orbitals np^6. The conduction band is comprised of np orbital of B cation and np^6 orbital of halide site[20], it is mostly contributed by Pb p state due to the dual nature of perovskite electronic structure, which exhibits both ionic and covalent characteristics[64,65].

In recent years, the bandgap tunability property has been extensively investigated by compositional engineering methods for particular applications including indoor photovoltaic application and perovskite tandem solar cells[66,67]. Since conduction band is mostly determined by p state of metal cation, Sn, with $5p$ orbital has been used to replace Pb, which has $6p$ orbital, partially to reduce the bandgap for bottom sub-cell in a tandem solar cell[68]. Since $5p$ orbital has lower energy compared to $6p$ the conduction band is lowered and hence perovskite bandgap is reduced. The highest performance single-junction Sn-Pb perovskite has achieved a bandgap of 1.25 eV with the composition $FA_{0.6}MA_{0.4}Sn_{0.6}Pb_{0.4}I_3$, the PCE of it has reached 17.8% and the corresponding 2-terminal tandem cell has reached PCE >30%[69].

The valence band shift is used more commonly for indoor photovoltaic research. We have discussed in Section 1.3 that indoor light sources have much narrower

illumination spectra compared to sunlight. For perovskite materials which normally have a bandgap of 1.5-1.6 eV, the absorption wavelength range is too wide and does not match with the narrow indoor illumination spectrum. The mismatch does not contribute to photocurrent and resulted in V_{OC} loss due to narrow bandgap. In this case, it becomes an important topic to widen the bandgap to eliminate the negative effects. For standard perovskite methylammonium lead iodide (MAPbI$_3$), it has I ($5p^6$) at its halide site and the bandgap is 1.56 eV, when I is substituted by Br ($4p^6$) and Cl ($3p^6$), the valence band is lowered significantly by 0.86 eV and conduction band is also increased slightly by 0.26 eV[70]. The band diagram shift is exhibited in **Figure 1-9 (c)**.

Halide substitution plays an important role in indoor photovoltaic development, but to obtain a reliable composition that gives ideal PCE or stability, the composition should not be tuned casually, as there are various strains, i.e. maintaining homogeneous morphology, avoiding phase segregation, or defects controlling, need to be considered. In this case, some advanced methods of compositional tuning and an overall vision of perovskite indoor photovoltaic development will be presented in Section 1.6.
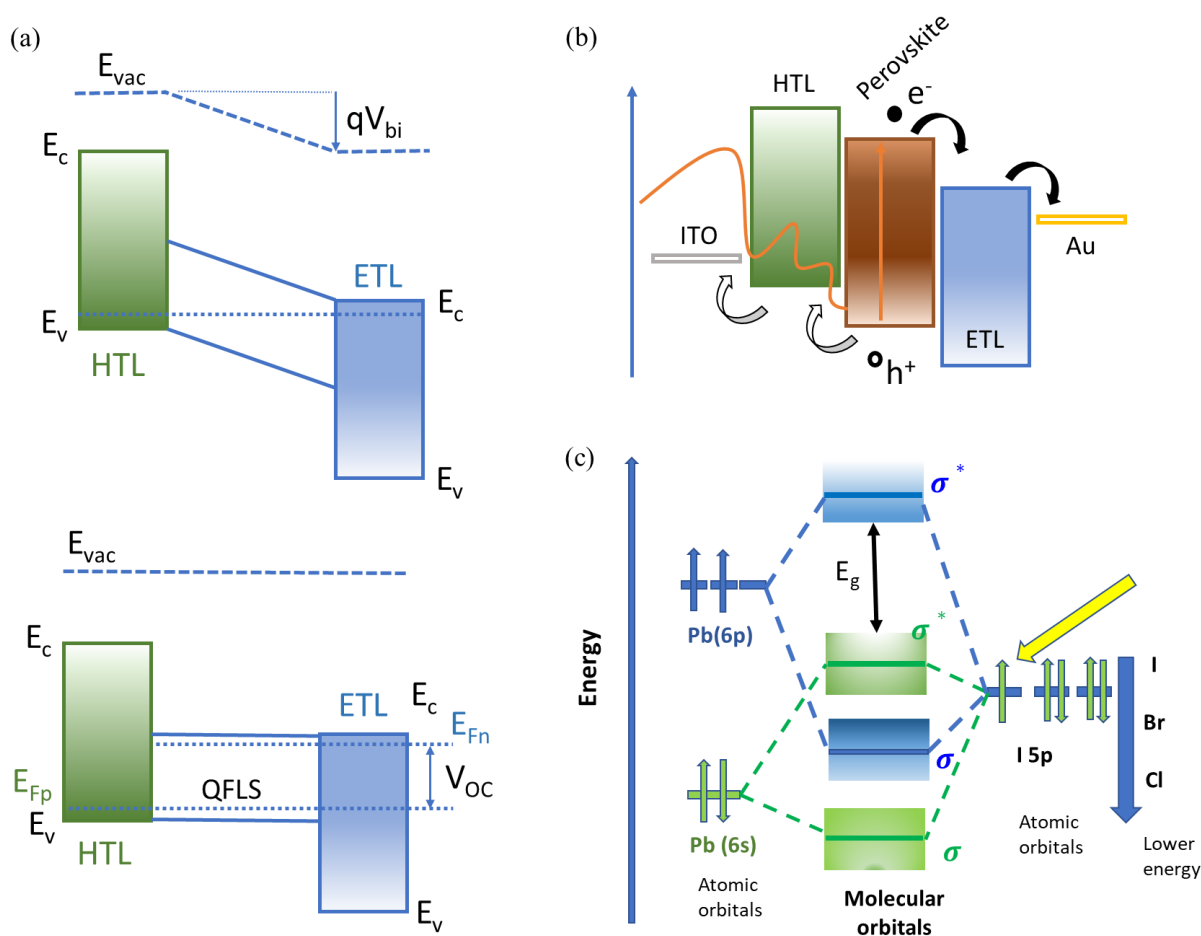
Figure 1-9: (a) Band diagram of p-i-n photovoltaics under short-circuit condition and open-circuit voltage conditions[60]; (b) illustration of charge transport of a p-i-n cell; (c) band structure of perovskite[20].

1.5.5. Recombination and Defects of Perovskite Indoor Photovoltaics

When a perovskite solar cell is exposed to light, photons with higher energy than the band gap will be absorbed and generate hole-electron pairs. Some electrons will be excited to higher energy level positions than the band edge of conduction band, and immediately relaxed down to the band edge in most typical metal halide perovskites due to low exciton binding energy[71,72]. Charge carrier lifetime refers to the period that how long the electrons and holes can maintain at conduction band and valence band before recombination, which plays determined role in solar cell performance[73]. The

recombination of charge carriers in a semiconductor can be summrised by the following equation[74]:

$$-\frac{dn}{dt} = k_1 n \times k_2 n^2 \times k_3 n^3 \qquad (1\text{-}16)$$

where n refers to charge carrier density, k_1 represents the first-order non-radiative trap-assisted recombination as shown in **Figure 1-10 (a)**, this includes trap-assisted Shockley-Read-Hall (SRH) recombination at the bulk and interface recombination. SRH recombination is mainly attributed to uncoordinated ionic defects of perovskite-induced deep level trap states. Interface recombination happens at interfaces between perovskite and charge transport layers due to the energy gap between each layer as shown in **Figure 1-10 (b)**[75]. k_2 is the second-order band-to-band radiative recombination constant as shown in **Figure 1-10 (c)**; k_3 is the Auger recombination rate constant, Auger recombination refers to the excess energy from electron-hole recombination is delivered to other electrons and holes to excite them to higher energy states as illustrated in **Figure 1-10 (d)**[76,77]. For MAPbI₃, the commonly studied metal halide perovskite, the recombination within the thin film is dominated by k_1 when the photoexciton densities is below 10^{15} cm^{-3}, k_2 dominates recombination in the range of ~10^{15} – 10^{17} cm^{-3} and k_2 dominates when photoexciton densities larger than 10^{17} cm^{-3}[78]. The steady state carrier population for a perovskite solar cell under operation under AM 1.5G irradiance is in the range of ~10^{15} – 10^{16} cm^{-3}, hence the majority of recombination types are trap-assisted recombination and band-band radiative recombination, which should be carefully coordinated to improve the performance of solar cells[79]. The trap-assisted recombination should be miminised by reducing the defects within devices to achieve better performances*. For solution-processed perovskite thin films, the trap density is reported ranging from 10^{14} – 10^{17} cm^{-3}, which is comparable to the excited charge carrier density (10^{15} – 10^{16} cm^{-3} under AM 1.5G)[80,81]. However, perovskite solar cells can still provide exceptional high PCE up to 26.1% under ultra-thin device architecture with long charge carrier lifetime above 100 ns[82]. This could be attributed to the defect tolerance nature of perovskite materials that most intrinsic defects exist either beyond the bandgap or close the conduction or valence band edges[83–85]. These shallow traps could be filled by solar fluences and be less detrimental to solar cell performance. However, for indoor photovoltaic operating at dim-light of which the light intensity is almost 3 orders lower compared to AM 1.5G

1 sun light, the defects may not be fully passivated by the light fluences hence a higher ratio of charge carriers could be trapped. The charge carrier density for perovskite indoor photovoltaics have not been systematically reported but should be 1 or 2 orders of magnitude lower than under 1 sun-based irradiance[86]. In this case, reducing defects in device fabrication is particularly crucial to improve the indoor photovoltaic performance. Efforts have been taken to reduce the defects at perovskite bulk or at grain boundaries by improving crystallisation and morphology of thin films[87,88]. More recently, the importance of interfaces in PSCs is gradually revealed and emerging interlayer passivation methods have been developed have been made to reduce the non-radiative recombination at interfaces of perovskite solar cell devices[89,90]. It is found that the recombination loss for a PSC device is dominated by the non-radiative recombination at interfaces between perovskite and charge transport layers, which emphasise that developing efficient interfacial strategies is more crucial for PSC development[91]. A detailed discussion of defect passivation methods for bulk and interfaces for state-of-art indoor perovskite photovoltaics is done in the following section 1.6.
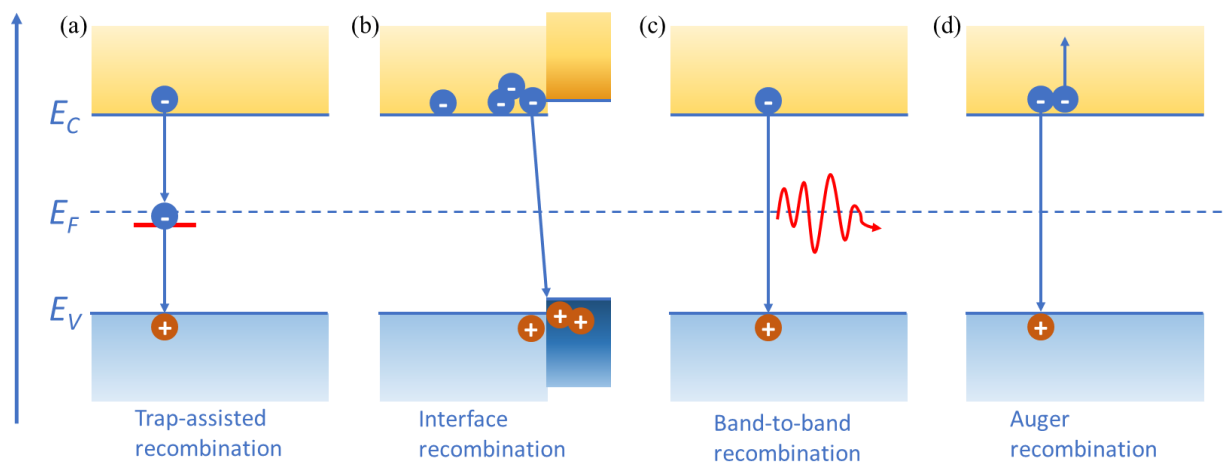

Figure 1-10: Different types of recombination processes within solar cells (a) Trap-assisted recombination; (b) interface recombination; (c) band-to-band radiative recombination; (d) Auger recombination.

1.6. State-of-art of Perovskite Indoor Photovoltaics

Recent years have witnessed rapid progress in indoor PV, as discussed in Section 1.1, different types of PV materials including Si, III–V, CIGS, organic, dye-sensitized, and halide perovskite have been considered as promising candidates for indoor PV research and market[92–96]. The crystalline and microcrystalline silicon PVs, exhibit only low power conversion efficiency (PCE) (~9%) due to their non-ideal bandgap and defects[26,97,98]. However, a PCE of 36% has been recently reported for hydrogenated amorphous silicon (a-Si:H) thin film solar cells under white LED illumination of 3000 lux[92]. III–V materials based solar cells have achieved a higher PCE of 21% under indoor white LED light, with $Al_{0.2}Ga_{0.8}As$ as the active layer[95]. However, the high fabrication cost of III–V materials hinders their further application for the PV industry, especially for wide-area devices[26,99]. Superior efficiencies have been achieved by the solution-based PVs: dye-sensitized solar cells (DSSC)), organic photovoltaics (OPV) and halide perovskites[100–104]. Recently Lee *et al* have demonstrated a PCE of 30% under 500 lux LED illumination for the OPVs[100]. DSSCs with 25% PCE under 900 lux fluorescence lamp illumination were also recently reported[104]. However, the limited selection of dye and liquid electrolytes are the remaining problems to improve the stability and reduce the fabrication cost for DSSC[105]. The sensitivity to moisture, and oxygen and the high cost of photoactive materials for OPV also challenge their application for indoor PVs[106].

For indoor perovskite photovoltaics, most of the initial publication of perovskite IPV is based on the standard $CH_3NH_2PbI_3$ composition. By trap controlling and carrier dynamic optimization approach such as employing interface engineering, we have seen an increasing trend of indoor perovskite photovoltaics PCE based on $CH_3NH_2PbI_3$ from 20% to 34%[107–109].

However, $CH_3NH_2PbI_3$ has a bandgap of only 1.56 eV. Based on our discussion in Section 1.3, it is significantly lower than the optimal bandgap (~1.9 eV) for indoor photovoltaic application. In this case, mixing halide ions in perovskites became a common and popular approach for compositional engineering to widen the band and it has been proved that good photovoltaic performance can be obtained by this method. Jagadamma et al. have achieved PCE of 23% by iodide-chloride and iodide-

bromide mixture under LED and compact fluorescent lamp[110]. Sun et al. has used composition $Cs_{0.05}MA_{0.95}PbBr_xI_{3-x}$ and achieved a bandgap shift from 1.6 to 1.75 eV. The solar cell efficiency has reached 36% for LED and 33.2% for CFL lamps. Film quality and band alignment are both improved with this halide composition tuning[111].

However, even though much progress has been made in iodide-bromide mixing, Hoke et al. reported that a larger amount of Br incorporation (larger than 20%) will result in phase segregation[112], which means charge carriers will be separated into I-rich and Br-rich domain, respectively. In this case, the excited electrons will relax down to the bandgap of I-rich domain and make the bandgap shift noneffective anymore, hence V_{OC} is limited. Although phase segregation is only mentioned in high light intensity conditions (~10% of solar illumination) up to now, it is still important to avoid this negative phenomenon under indoor conditions. In this case, Xu et al. has reported a triple-anion alloying method in which incorporating Cl into I-Br mixed halide perovskite could suppress phase segregation effectively by modifying morphology and surface passivation[113]. It is observed that moving from double-anion to triple-anion perovskite enhanced charge carrier lifetime as a factor of 2 and suppressed light-induced phase segregation up to 100 suns, the bandgap of this triple-anion perovskite reached 1.67 eV, which makes triple-anion a promising method for indoor photovoltaic research. Cheng et al. have reported that triple-anion $MAPbI_{2-x}BrCl_x$ perovskite indoor photovoltaic cell has achieved a high V_{OC} of 1.028 V and highest PCE of 36.2% under 1000 lux fluorescent light[30]. Nochang Park and co-workers have found that chlorine doping in triple anion perovskite facilitates hole extraction on its top surface and contributes to suppression of ion migration and non-radiative recombination, which is crucial for indoor photovoltaic applications[114].

Defect controlling to minimise non-radiative recombination is important, since low indoor light intensity generates a smaller amount of charge carriers, trap-induced recombination will be more prominent since a higher ratio of charger carriers could be trapped by defects[30]. Trap controlling for better performed perovskite solar cells is already an extensively studied area, which leads to the emergence of interfacial passivation. Interfacial passivation refers to the approaches that introducing an interlayer at the top surface or buried interface between perovskite and transport layers. One common method is to introduce a two-dimensional perovskite thin layer

(e.g., PEA_2PbI_4) at the top surface of perovskite to create a 2D/3D structure to passivate interfacial defects and suppressing non-radiative recombination[115]. Zheng Xu and co-workers introduced organic halide PEACl to the perovskite/Spiro-OMeTAD interface, it is found PEA^+ provided improved stability as organic intercalation and Cl^- ions diffuse to passivate defects which results in exceptional high V_{OC} of 1.15 V and PCE of 21.49%[116]. Another efficient interfacial passivation method is to introduce an ultra-thin self-assembled monolayer (SAM) at interfaces or serves as novel hole selective layers directly. Li et al introduced [6,6]-4-fluorophenyl-C_{61}-butyric acid (FPAC$_{60}$) at the buried interface between SnO_2 and perovskite, it is found that FPAC$_{60}$ could not only passivate defects but act as nucleation site to regulate the crystallisation of perovskite[117]. Albrecht et al. have introduced (3,6-dimethoxy-9H-carbazol-9-yl)ethyl]phosphonic acid) (MeO-2PACz) as HTL in p-i-n devices, the MeO-2PACz provides suitable band alignment, and suppression of non-radiative recombination and leakage current, which is now the most extensively used SAM material[118].

Besides the interfacial defects, defects in bulk material also plays crucial role determining device performance, e.g., methylammonium vacancies, these could be overcome by additive engineering to the perovskite precursor. Wu et al. introduced 2-hydroxypropyl β-cyclodextrin (HPβCD) and 1,2,3,4-butane tetracarboxylic acid (BTCA) directly into perovskite precursor to form built-in supramolecular complex, the high density of hydroxyl and carboxyl group can readily bond to Pb^{2+} and coordinate crystallisation, which results in less defect density and higher carrier mobility, with additional effect to prevent lead leakage[119]. Li et al introduced bis-adduct2,5-(dimethylester)C_{60}fulleropyrrolidine (bis-DMEC$_{60}$), which could diffuse into grain boundaries and passivate defects, resulting in exceptional 22.58% PCE[117]. He et al. introduced rubidium (Rb) to fill the A-site vacancy caused by methylammonium vacancies, which alleviates shrinkage strain of perovskite crystal, resulting homogeneous perovskite film with excellent PCE of 21.72% and V_{OC} of 1.22 V for wide-bandgap PSC (1.68 eV)[120].

The abovementioned defect passivation methods provide a roadmap for indoor photovoltaics to address the detrimental effects of higher charge carrier trapping under dim light. It is seen that these approaches implemented to indoor photovoltaic application successfully. Dagar et al. introduced a MgO interlayer at buried interface

between SnO_2 and perovskite surface in n-*i*-p device architecture, the modification resulted in more uniform films, reduced interfacial recombination contributed to high stability and achieved high PCE of 26.9%[109]. Li et al. introduced 1-butyl-3-methyllimidazolium tetrafluoroborate ([BMIM]BF$_4$) ionic liquid into $PC_{61}BM$/Ag interface to passivate interface defects and resulted in exceptional high PCE of 35.2% under indoor condition[121]. Actions have also been taken from perspective of transport layers. Wong et al. have added Dithieno[2,3-d:2′,3′-d′]thieno[3,2-b:3′,2′-b′]dipyrrole (DTPT)-based acceptor-donor-acceptor (A–D–A) molecules as electron-donating core into PCBM to create a PCBM:DTPTCY blend, passivating interfacial defects and facilitating hole extraction[122]. In addition, 2D/3D perovskite structure at interfaces have also been investigated. Particularly, the wide-bandgap nature of 2D perovskites could blue-shift the absorption spectrum of perovskite layer, which benefits the light harvesting of indoor light. Brown et al. introduced tetrabutylammonium bromide (TBAB) between the perovskite and Spiro-OMeTAD to passivate defects, the absorption edge is shifted from 775 nm to 760 nm. The TBA$^+$ cation intercalates into the structure and substituting FA$^+$ cation to form 2D structure, resulting improved carrier mobility and 3 times lower defect densities, leading to 32.5% PCE on flexible substrates under 1000 lux cool white LED light[123]. Liu et al. have introduced β-alaninamide hydrochloride (AHC) to spontaneously form a layer of 2D perovskite nucleation seeds for improved film uniformity, crystallization quality, resulting in excellent PCE of 42.12% under 1000 lux warm LED light[124].

The abovementioned work is focused on interface engineering and can significantly reduce trap density at interfaces, but defects that lie deep in the bulk material also need to pay attention. Wang et al. replaced DMF with N-methyl-2-pyrrolidone (NMP) in perovskite precursor, significantly passivated intrinsic defects in bulk film with the assistance of coordinate between NMP and excess PbI$_2$ and ion vacancies[125]. He et al. has very recently reported that a holistic method to reduce the defect level at interface and bulk material simultaneously. By employing guanidinium into perovskite bulk film and 2-(4-methoxyphenyl)ethylamine hydrobromide (CH$_3$O-PEABr) for surface passivation, the traps states at the interface and bulk film are effectively reduced, this approach resulted in a high V_{OC} of 1.00 eV and the excellent PCE of 40.1%[126]. The record efficiency of indoor perovskite photovoltaics is also achieved by additive engineering for bulk defect passivation, Mai et al. introduced oleylammonium

iodide solution in trichloromethane as dual additives into the perovskite precursors to improve the affinity and interaction with contact substrates for the growth of perovskite crystals. A record indoor PCE of 44.72% is achieved under 1000 lux U30 light (338.2 μW cm^{-2})[127].

1.7. Scope of the Thesis

The thesis focuses on fabricating efficient and reliable indoor perovskite photovoltaic devices and understanding the corresponding perovskite thin film properties and device physics. This includes understanding the properties of device architectures under low intensity indoor light, perovskite bandgap optimisation, charge transport behaviour and interlayer modification, and sensor powering for IoT applications. To complete this comprehensive study, a wide range of processing and characteristic techniques are used, including perovskite thin film and transport layer synthesis and deposition, thin film characterisations to understand the morphology, crystallography and crystallisation (e.g. SEM, XRD and PL) kinetics and device characteristics to understand the charge carrier dynamics. This thesis extends from perovskite thin films to completed cells and by linking the properties of thin films or devices to the measured photovoltaic performances, this study could provide a comprehensive understanding to develop high-quality indoor perovskite photovoltaic devices that could assist to developing promising self-powered microelectronic devices to achieve the vision of IoT.

Device Architecture It is discussed in Section 1.5.2 that both n-i-p and p-i-n are critical device architectures for perovskite solar cells. Since different transport layers are used for different architectures, the energy alignment and interfacial conditions are different and the behaviours of different architecture of perovskite photovoltaic devices are yet to be understood. It is important to reveal the relationship between the indoor photovoltaic performances and device physics under low light indoor lighting conditions. In this case, we compare the 1 Sun (100 mW/cm2) and indoor light (0.3 mW/cm2) harvesting properties of n-i-p and p-i-n architecture halide perovskite photovoltaic devices using CH$_3$NH$_3$PbI$_3$ as the photo-active layer. In addition to the photovoltaic performances, light intensity-dependent photovoltaic performance parameters (open-circuit voltage and fill factor) of these devices reveal the existence

of trap assisted recombination losses and charge extraction barrier in the n-*i*-p devices limiting their performance under low-intensity illumination. This reveals the importance of independently optimising the halide perovskites indoor photovoltaics from that of 1 sun illumination, for maximising the indoor light-harvesting and to reliably power the sensors in the IoT system.

In addition, it is important to bring *J-V* hysteresis behaviour of halide perovskites indoor PVs under indoor lighting into sight. The hysteresis refers to the phenomena that the *J-V* curves obtained from the forward voltage scan (short-circuit to open-circuit) and reverse voltage scan (open-circuit to short-circuit) differ considerably resulting in different PCE values which detrimentally influence the reliability of measurements and powering of the low power electronic components in the IoT technology. When I started my PhD research, most publications of indoor perovskite photovoltaics only include single scan *J-V* curves without mentioning the hysteresis behaviour of the steady state PCE. However, although hysteresis behaviour is already widely studied under 1 sun condition, it is critical to understand it under indoor lighting conditions due to low light intensity and spectral differences. There existed a knowledge gap in the hysteresis behaviour of these photovoltaic devices under indoor lighting conditions. Hence, the degree of hysteresis in halide perovskite indoor photovoltaic devices is explored by carrying out both transient *J–V* scan and steady state maximum power point tracking (MPPT) measurements. It was observed that the divergence of the PCE values estimated from the *J–V* scan measurements, and the maximum power point tracking method is larger under indoor illumination compared to 1 sun, and hence established that for halide perovskite-based indoor PV, the PCE from the MPPT measurements should be prioritized over the *J–V* scan measurements.

Charge Transport Layer Properties The different properties of device architecture emphasise the importance of selection of charge transport materials. Despite the promising attributes of commonly used charge transport layers under 1 sun including Spiro-OMeTAD, P3HT, Poly-TPD and NiO, their performance comparison under indoor lighting conditions is still ambiguous. The lower illumination intensity and different light spectrum necessitates the separate optimisation of not only the active layer but different charge transport layers as inappropriate transport and charge selectivity can cause dramatic adverse effects on the performance of perovskite IPVs

due to the much lower photogenerated charge carrier density under indoor low light conditions. In this case, the device performances and device physics of photovoltaic devices using different charge transport layers are studied. Based on these results, the relationship between transport layers and the interfacial conditions can be revealed. The buried interfacial conditions can determine the overall photovoltaic device efficiency and hence understanding their characteristics is important to develop the effective mitigation methods. In order to passivate defects and obtain better performed devices, novel interlayer is introduced to coordinate the interfacial conditions, which could be a critical method to improve the performances of metal oxide transport layer-based indoor perovskite photovoltaics.

Bandgap Tuning In section 1.3, we discussed the need of wide-bandgap perovskites for promising indoor photovoltaics. The bandgap of perovskites can be tuned by compositional engineering and has already been widely studied for normal perovskite solar cells. However, wide-bandgap perovskite could rise several challenges including poor crystallisation or phase segregation, which is detrimental to device performances. In this case, the strategy to develop high quality wide-bandgap perovskite and the role of the novel wide-bandgap perovskite in determining the performances in indoor photovoltaics needs to be investigated. In this case, a triple anion alloying which combines three halides (I, Br and Cl) is developed. The perovskite film quality, optical absorption, composition, microstructure, crystallinity, morphology and crystallisation is process is investigated. Importantly, the triple anion perovskite improves the indoor devices performances significantly, and various characterisations have been done to understand the device physics and its functionality. Particularly, we investigated the role of unstable Cl content in this triple anion perovskite system. This study could provide a comprehensive image to apply triple anion wide-bandgap perovskite for developing promising indoor photovoltaics in research field and industry.

Sensor Powering The ultimate goal of developing highly efficient indoor photovoltaic devices is to develop promising self-powered microelectronic sensors for IoT applications. In this case, it is urgent to understand whether the developed indoor perovskite photovoltaics are reliable to power a microelectronic device. In this case, we developed 3 different strategies to investigate the feasibility of using our devices for sensor powering. We have successfully powered lab-based and commercialised

sensor using direct connection, Arduino based controlling and remote controlling, which proves the superiority of the developed indoor perovskite photovoltaic devices and is a crucial step towards the real-life applications.

Chapter 2

Experimental Methods

2.1. Materials and device fabrication

2.1.1. Materials

Perovskite materials CH_3NH_3I was purchased from Greatcell solar. PbI_2, $PbBr_2$ and $PbCl_2$ were purchased from Alfa Aesar.

n-*i*-p transport layer materials SnO_2 solution (CAS 18282-10-5) for the electron transport material was purchased from Alfa Aesar and diluted in deionized water with a volume ratio of 1:6.5 before spin coating. Hole transport materials including [2,2',7,7'-Tetrakis[N,N-di(4- methoxyphenyl)amino]-9,9'-spirobiflourene (Spiro-OMeTAD, >99% purity), 4-tert-butyl pyridine (tBP, 96% purity), lithium-bis(tri-fluoromethanesulfonyl)imide (Li-TFSI, 99.95% purity) and tris(2-(1H-pyrazol-1-yl)-4-tert-butylpyridine)cobalt(III) tri[bis(trifluoromethane)sulfonimide] (FK 209) were purchased from Ossila, Sigma Aldrich and Greatcell Solar Materials, respectively. Poly (3-hexylthiophene-2,5-diyl) (P3HT) was purchased from Sigma Aldrich.

p-*i*-n transport layer materials Electron transport materials bathocuproine (BCP) was acquired from Sigma Aldrich (99.99% purity), and $PC_{60}BM$ was from American Dye Source Inc. Hole transport materials poly(4-butyltriphenylamine) (poly-TPD) was aquired from American Dye Source Inc., poly[(9,9-bis(3'-(N,N-dimethylamino)propyl)-2,7-fluorene)-alt-2,7-(9,9-dioctylfluorene) (PFN) was bought from 1 Materials. 2PACz ([2-(9H-carbazol-9-yl)ethyl]phosphonic acid) was purchased from Tokyo Chemical Industry. Nickel oxide was purchased from Avantama AG. Copper (ii) acetylacetonate ($Cu(acac)_2$, purity >99.9%) was purchased from Sigma Aldrich.

Solvents dimethyl sulfoxide (DMSO, anhydrous, ≥99.9%), N,N-dimethylformamide (DMF, anhydrous, 99.8%), chlorobenzene (anhydrous, 99.8%), chloroform (anhydrous, 99.8%), methanol (anhydrous, 99.8%), acetonitrile (anhydrous, 99.8%), and diethyl ether (anhydrous, ≥99.7%) were purchased from Sigma Aldrich.

2.1.2. Solar cell device fabrication

In this thesis, solar cell devices were fabricated with n-*i*-p and p-*i*-n devices, respectively. The specific device structure and transport/extraction layers were shown in **Figure 2.1**. Spin-coating and thermal evaporation are key techniques in the processing of solar cell devices.

Spin-coating Spin-coating is one of the most common techniques to deposit thin films to substrates. Spin-coating is carried out by adding the coating solution onto the surface of the substrate on a spin coater followed by high-speed spinning rotating of the substates, which substrates spreads out the solution to create an even covering on the substrates under the pulling of centripetal force and surface tension. The formation of thin film can be divided into several stages. Firstly, the solution is cast onto the substrate at the status either the substrate is already spinning or is static, the solution is spread across the substrate due to centrifugal motion. While the substrate is then spinning, most of the solution is expelled from the substrate, the remaining fluid then begins to thin, which is dominated by viscous forces and create thin films.

Anti-solvent treatment is applied during spin-coating to facilitate crystallisation. Anti-solvents are fluid that less soluble to the solutes, which removes residual solvents and facilitate fast crystallisation and film formation.
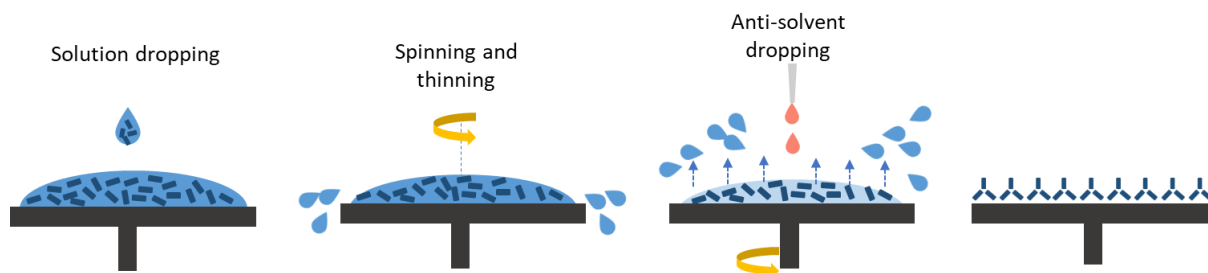
Figure 2-1: Schematic of spin-coating process.

Thermal evaporation Thermal evaporation is a common method to deposit top metal electrode carrying out under high vacuum ($<10^{-4}$ Pa). A source material (Au or Ag) is placed into a tungsten charge holding boat, which is then exposed to large direct current (DC) to reach the high melting point of metals. The high vacuum supports the evaporation of the metal and facilitates the vapor particles moving and directly reaching the substrates, where the vapor transfers to solid state and form a thin layer of metal.
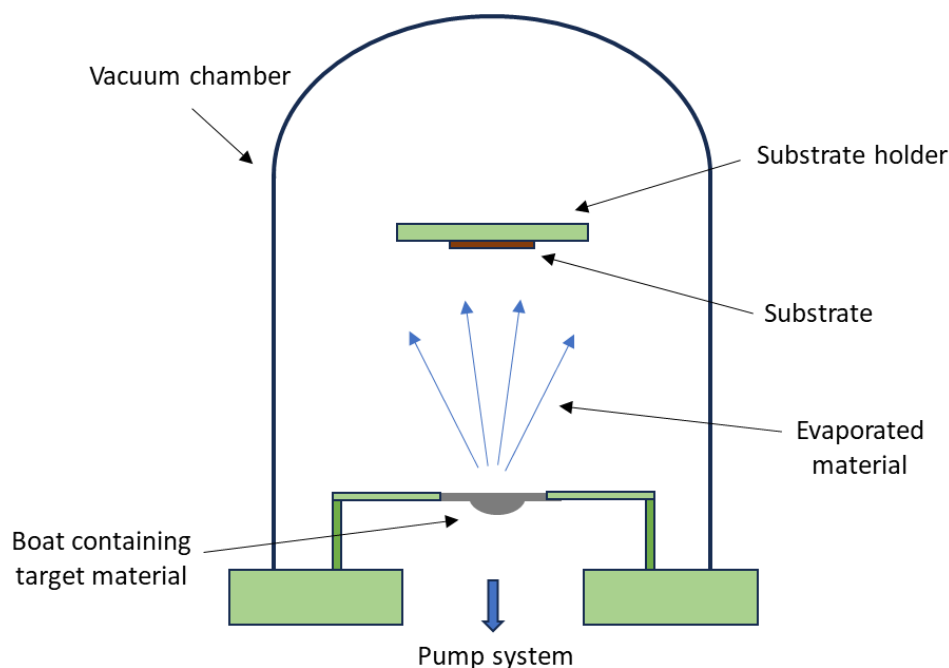

Figure 2-2: Schematic of thermal evaporator.

For n-*i*-p devices, pre-patterned indium tin oxide (ITO) coated glass substrates were sequentially cleaned by sodium dodecyl sulphate (SDS), deionized water, acetone and isopropyl alcohol, all with sonication. The substrates were then cleaned with oxygen plasma for 3 minutes with a Plasma Asher. 100 µL SnO_2 solution was deposited onto

the cleaned substrates by spin-coating at 3000 rpm for 30 seconds, followed by 150°C thermal annealing for 30 minutes to form a compact hole-blocking SnO_2 layer. To prepare $CH_3NH_3PbI_{2.6}(BrCl)_{0.2}$ triple anion perovskite precursor solution, CH_3NH_3I (1 M; 159 mg), $PbBr2$ (0.1 M; 36.7 mg), $PbCl_2$ (0.1 M; 27.8 mg) and PbI_2 (0.8 M; 368.8 mg) were dissolved in 66 µL of DMSO and 636 µL of DMF and stirred for 1 hour. To prepare $CH_3NH_3PbI_3$ perovskite precursor solution, CH_3NH_3I (1 M; 159 mg) and PbI_2 (1 M; 461 mg) were dissolved in 66 µL of DMSO and 636 µL of DMF and stirred for 1 hour. For the deposition of TA and $CH_3NH_3PbI_3$ perovskite active layer, 90 µL of perovskite precursor solution was deposited onto the SnO_2/ITO/glass substrates at 4000 rpm for 30 s, a diethyl ether (DEE) anti-solvent washing was carried out for TA perovskite layer fabrication at the first 5th second during spin-coating. For $CH_3NH_3PbI_3$ layer the anti-solvent washing time is at the first 7th second. The spin-coated films were treated by a thermal annealing under vacuum for 1 minutes, followed by an ambient N_2 thermal annealing for 2 minutes in a nitrogen glove box. For the TA devices of thermal annealing time variation, the ambient N_2 annealing time was adjust accordingly to 10 minutes, 30 minutes, 45 minutes and 1 hour.

For the preparation of the hole transport layer 72.3 mg Spiro-OMeTAD was dissolved in 1 mL chlorobenzene, mixed with 28.8 µL tBP, 17.5 µL Li-TFSI (52 mg Li-TFSI in 100 µL acetonitrile) and 29 µL FK209 (30 mg FK209 in 100 µL acetonitrile), 55 µL of prepared HTL solution was spin coated onto the perovskite layer at 4000 rpm for 30 seconds. The glass/ITO/SnO_2/perovskite/Spiro-OMeTAD samples were wrapped in aluminum foil and left overnight in a dessiccator at room temperature for oxygen doping of Spiro-OMeTAD. Finally, a 60 nm thick Au electrode was thermally evaporated (chamber pressure 3×10^{-6} mbar) on top of the HTL to complete the perovskite solar cell device.

For organic extraction layers for p-i-n devices, 1.4 mg Poly-TPD was dissolved into 1 mL and stirred continuously for 4 hours under room temperature, 100 µL Poly-TPD was spin-coated onto the cleaned ITO substrate at 6000 rpm for 30 s. 1 mg PFN-P1 was dissolved into 995 µL methanol, stirring for 2 h under 60 °C, then 5 µL acetic acid was added and stirring for another 2 h under 60 °C. 100 µL PFN was spin-coated on top of Poly-TPD at 3000 rpm for 30 s. For the metal oxide extraction layers, NiO suspension was prepared by diluting 2.5 wt% nanoparticle solution using ethanol at a

ratio of 1:10. 2 mg Cu(acac)2 was dissolved into 1 mL chloroform under room temperature for 3 h. CuO_x film was prepared by spin-coating 90 µL Cu(acac)$_2$ solution at 2000 rpm for 30 s, following 120 °C annealing for 20 min. The film was then washed with 2 mL anhydrous methanol and cleaned by UV Ozone cleaner for 20 min. For 2PACz solution, 2.75 mg 2PACz was dissolved into 1 mL methanol, stirring at 38 °C for 15 min. 100 µL 2PACz solution was spin-coated on top of metal oxide extraction layers at 3000 rpm for 30 s, followed by 100 °C thermal annealing for 10 min. The MAPbI$_3$ perovskite film was then spin-coated on the top of PFN layer with the same conditions as n-i-p devices. For hole extraction layers, 13 mg PC$_{60}$BM was dissolved into 1 mL chlorobenzene, stirring at 60 °C for 4 h. The PC$_{60}$BM solution was filtered with 0.2 µm filter before use. 100 µL PC60BM was spin-coated at 1000 rpm for 60 s, annealing at 80 °C for 5 min. BCP solution was prepared by dissolving 0.5 mg BCP into 1 mL anhydrous ethanol, stirring at room temperature for 4-5 h. 100 µL BCP was spin-coated on top of PC60BM at 4000 rpm for 30 s. Finally, 100 nm Ag electrode was deposited on the top by thermal evaporation.
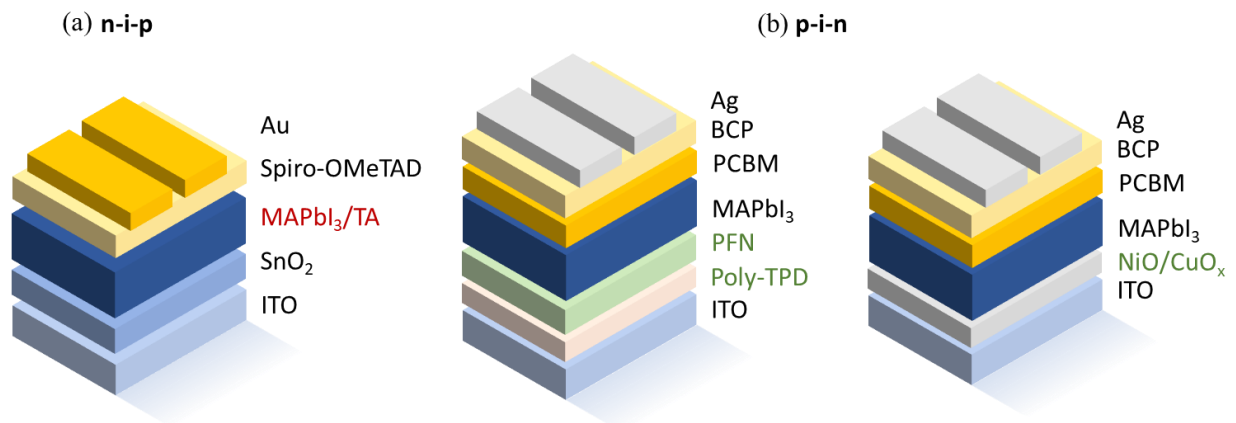

Figure 2-3: Device architecture of perovskite photovoltec cells fabricated in this thesis; (a) planar n-i-p and (b) p-i-n.

2.2. Thin film materials characterisation

2.2.1. Dektak stylus profilometer

The Dektak XT operates as a stylus profilometer, employing a diamond-tip stylus to contact with the sample. It applies a consistent stylus force while the sample stage moves the specimen beneath the stylus tip to record its profile. The Dektak is designed to analyse surface topography, enabling the measurement of step heights/thickness and lateral dimensions of features present on the sample. Additionally, it can assess surface roughness within a range of approximately 15 Å. Dektak stylus profilometer is used to determine the thickness of perovskite thin film.
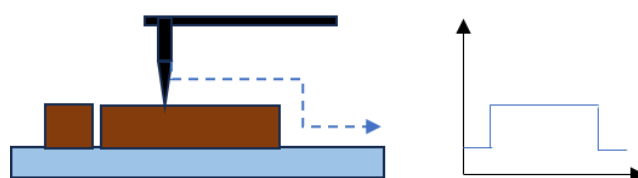

Figure 2-4: Dektak stylus profilometer schematic for thickness instrument.

2.2.2. Ultraviolet-visible spectroscopy (UV-Vis spectroscopy)

UV-Vis spectroscopy refers to absorption spectroscopy to obtain the absorbance spectra of a compound in solution or as a solid[128]. UV-Vis spectroscopy is based on electronic transitions of molecules absorbing light that excite electrons from HOMO to LUMO level. The energy of photons of light should be equal to the energy gap between HOMO and LUMO to be absorbed by the compound[129]. During the measurement, UV-visible spectrophotometers pass a light source through a sample, while a detector positioned on the opposite side records the transmitted light as shown in **Figure 2-5**. The absorption measurement can be quantified by Beer-Lambert Law. *A* represents absorbance, I_0 represents the incident light intensity, *I* refers to transmitted light intensity.

$$A = log_{10}\frac{I}{I_0} \qquad (2\text{-}1)$$

In this PhD project, the UV–vis absorption spectra of perovskite thin films were recorded using a Cary 300 Bio Spectrometer over the wavelength range 300 – 800

nm. To calculate the absorption coefficient α, the thickness of $CH_3NH_3PbI_3$ and triple anion incorporated perovskite films were measured using Dektak 150 Stylus profilometer and found to be 350 nm.
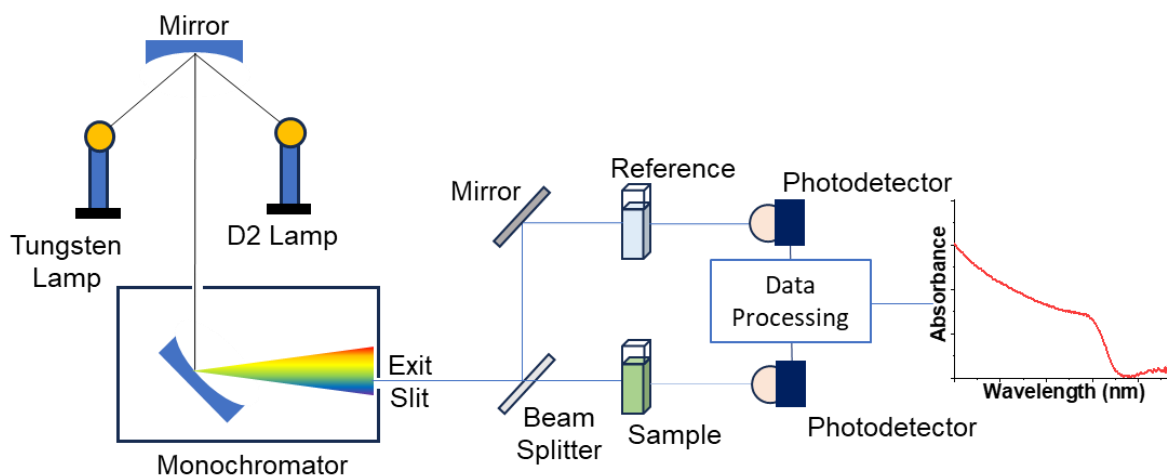

Figure 2-5: UV-Vis spectroscopy schematic for a double beam instrument. The tungsten lamp emits visible light and deuterium (D2) lamp emits emits ultraviolet light, the monochromator is used to generate light with specific wavelengths for the sample.

2.2.3. Ambient Photoemission Spectroscopy (APS)

APS measurement is used to measure the HOMO level of perovskite sample by detecting its ionization potential (work function) in ambient conditions. Ionization potential is the minimum energy required to remove the outermost electron. Ionisation potential measurements were made using an SKP5050 Scanning Kelvin Probe with an APS04 bolt-on module to perform ambient photoemission spectroscopy. This device uses a deuterium lamp with a built-in monochromator of 4-5 mm light spot which scans the sample using deep ultraviolet (DUV) light between 3.4-7.0 eV. A Schematic diagram of the APS system in shown in **Figure 2-6 (a)**. The photoemission yield is measured as current at the Kelvin probe tip.

The photoelectron emission and ion-current detection process can be divided into the following steps and is shown in **Figure 2-6 (b)**. (i) The DUV photons with higher energy than work function of the material ($E_{ph} \geqslant \Phi_m$) are absorbed by the surface of the material. The energy-provided electrons within the range of inelastic electron mean free path (escape path) will be emitted. (ii) The excited metal-photoejected electrons

are then subject to the image force due to the presence of the own electric field between the electron and the positively charged material. The image force extends to approximately 30 nm from the metal surface. (iii) An electron cloud is formed immediately outside the metal. The mean free path of electrons is 1-3 μm in ambient conditions. Inelastic scattering by much more massive N_2, O_2 and H_2O consumes the kinetic energy but preserves the charge of electrons. In this case, atmospheric ions including N_2^-, O_2^- and possibly OH^- are produced. (iv) Charged atmospheric ions drift towards the positively biased Kelvin probe tip. (v) The ion current is measured as a function of incident photon energy. When the energy is below the threshold of the work function, no emission takes place. While the photon energy is higher than the work function energy, ions will be induced and detected by the Kelvin probe tip and rise with the relation of $(E_{ph}-\Phi_m)^{1/3}$, which reveal the ionisation potential, and work function of the material[130].

The results can be easily interpreted in terms of Fowler Theory on photoemission, which describes the relation of quantum yield versus photon energy[131,132].

$$R \propto (E_{ph} - h\nu_0)^3 \qquad \text{(2-2)}$$

where R is the photocurrent per absorbed photon, E_{ph} is the photon energy, h is the Planck's constant and ν_0 is the threshold frequency. In this case, the cube root of the raw photocurrent data is then taken, in accordance with Fowler's theory of photoemission, before an extrapolation fit is performed on the linear region of the resulting data set. The intersection of this linear extrapolation with the baseline is the ionisation potential of the semiconductor being studied.
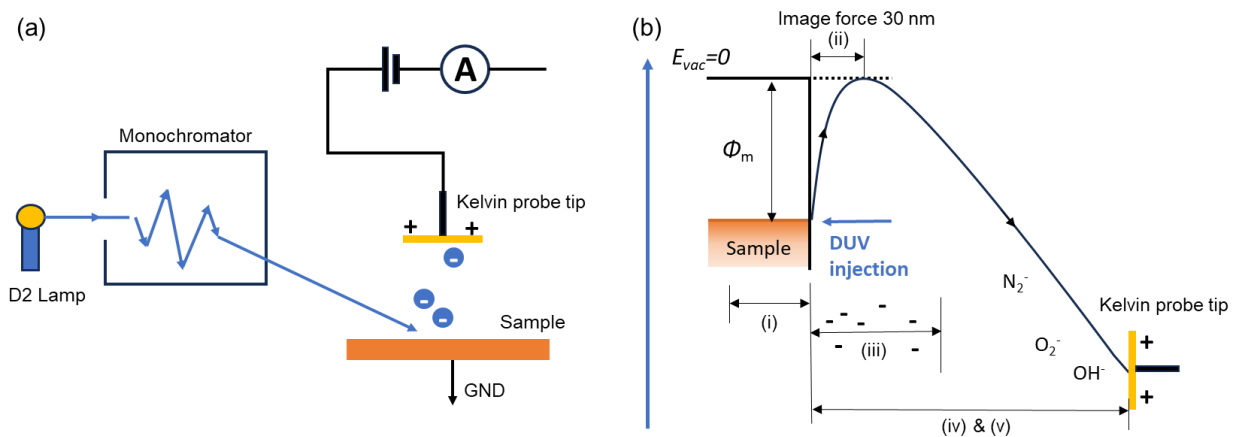
Figure 2-6: (a) Ambient photoemission spectroscopy schematic. (b) Illustration of working processes of ambient photoemission spectroscopy.

2.2.4. Scanning Electron Microscopy (SEM)

Scanning electron microscopy (SEM) is an approach creating images by capturing secondary electrons to show the morphology of a sample. A detector gathers electron signals from every pixel of the raster, enabling the creation of a point-to-point image on a display screen. It generates local images of a sample with large and flexible magnification ranges from ×10 to ×500000 which exhibits morphology situation in details.

When high energy electron beam is generated and hit the surface of a sample, elastic or inelastic scattering are produced. Elastic scattering generates backscattered electrons (BSEs), which are incident electrons scattered by atoms of the specimen. Inelastic scattering produces secondary electrons (SEs), which are ejected from the atoms of specimen. For SEs, electrons in an atom of specimen are given kinetic energy of incident electron and leave the orbital to become a secondary electron. SEs are typically deflected at small angles and show considerably low energy compared to incident electrons.

electrons emitted out from the surface and captured by Faraday cage with voltage ranges from -50V to +250V. Electrons captured are led to hit scintillator and generate photons which are then guided to photomultiplier tube as shown in **Figure 2-7**. An information transfer from electron energy to signal will occur and the signal will be enhanced ×10^6 inside the PM tube. In this case, images are formed by counting electrons at discrete points at sample, the brightness difference can be easily observed in terms of different amount of electron at each specific point. Electrons beam illuminates discrete area with probe diameter, d_f, and each point corresponds to a pixel of the image. An equation can be used to determine the relationship of pixel size to probe diameter.

$$M = \frac{L_{image\ monitor}}{L_{spec}} = \frac{d_{pixel}}{d_f} \qquad (2\text{-}3)$$

The SEM images of perovskite layers were taken using a Hitachi S4800 scanning electron microscope.
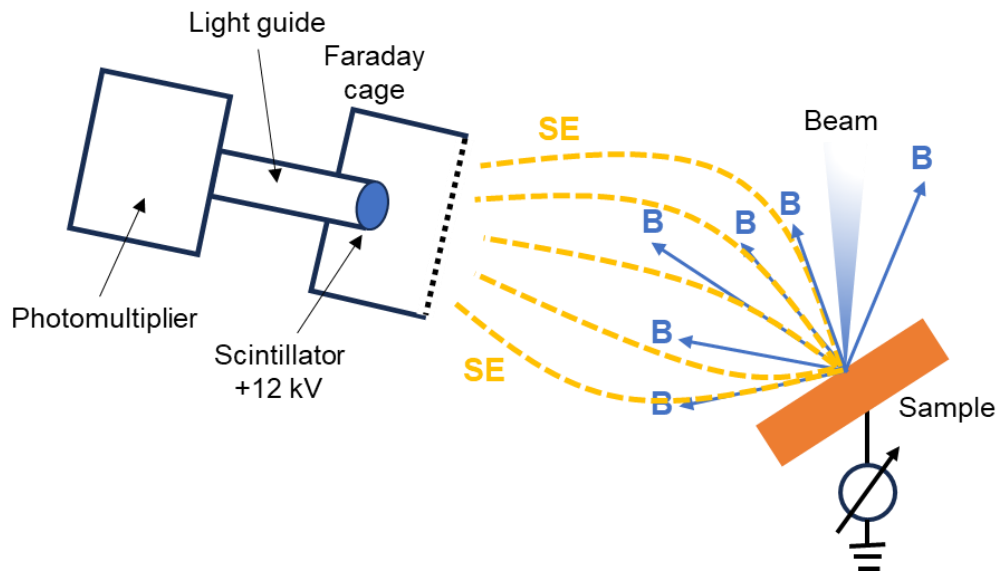
Figure 2-7: The detector signal collection of scanning electron microscopy. Bs are backscattered electrons. SEs are seconday electrons.

2.2.5. X-ray Diffraction (XRD)

X-ray diffraction (XRD) is used to detect crystal structure of a sample at atomic level. The equipment consists of three main parts: X-ray tube, sample and detector. The X-ray generated from the tube holds intrinsic oscillating electric field, when it inserts into a sample, X-ray will interact with orbital electron of the sample and induce oscillation of electrons, the oscillating electron then act as a source of electromagnetic radiation. Since the electrons move around the atomic nuclei via various orbitals, the X-rays will finally be scattered in all directions randomly. In this case, a spherical scattering wave is generated.

When considering the interactions between different atomics in the sample. The diffracted waves will interfere constructively or destructively with each other. And when the path difference of waves fits Bragg Law, there will be a constructive interference and a peak could then be detected in the spectra. The Bragg Law is exhibited below and illustrated in **Figure 2-8**, d_{hkl} represents the distances between lattice atomic planes, θ represents the angle of the incident beam and atomic planes, λ is the wavelength of the incident light.

$$2d_{hkl}\sin(\theta) = n\lambda \qquad \text{(2-4)}$$

When the equipment is operated, X-ray tube stay stationary, the sample rotates with specific angle rate, the detector will go through the measuring circle which arounds the sample. In this case, the spectra with scattering intensity versus 2θ can be obtained. since each material has a unique arrangement of planes and distances, thus every material has a unique XRD pattern and can be recognized as a "fingerprint". By comparing the XRD pattern, the existence of specific material can be identified.

X-ray diffraction spectra of the perovskite thin films were collected on Bruker D8 Discover (EIGER2R-500K 2d detector) instrument using Cu Kα1 (λ=1.54060 Å). Data were collected in the range 5° −60° 2θ with a step size of 0.02° and a time step of 1 s, cumulative time per step (2d detector) of 777 s.
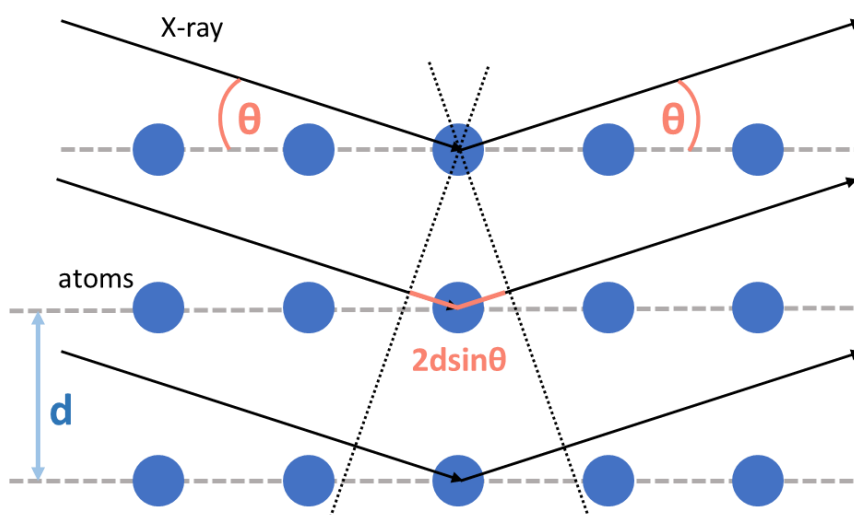

Figure 2-8: The illustration of Bragg Law using in X-ray diffraction.

2.2.6. In-situ Grazing Incident Wide-angle X-ray Spectroscopy (GIWAXS)

GIWAXS is a typical scattering technique to probe the thin film crystal structure[133]. in-situ GIWAXS can reveal structural revolution and crystallisation pathways in real time with synchrotron facility[134]. The schematic of measurement is shown in **Figure 2-9**. During the measurement, an X-ray beam with wave vector $\vec{k_i}$ incident the sample with grazing angle α_i, a scattered wave $\vec{k_f}$ is generated and collected by detector. The scattered wave vector $\vec{q} = \vec{k_f} - \vec{k_i}$ can be described by the following equations[135,136]:

$$\overrightarrow{q_x} = \frac{2\pi}{\lambda}\left(cos\alpha_f\ cos\varphi - cos\alpha_i\right) \qquad \text{(2-5)}$$

$$\overrightarrow{q_y} = \frac{2\pi}{\lambda}\left(cos\alpha_f\ cos\varphi\right) \qquad \text{(2-6)}$$

$$\overrightarrow{q_r} = \sqrt{q_x{}^2 + q_y{}^2} \qquad \text{(2-7)}$$

$$\overrightarrow{q_z} = \frac{2\pi}{\lambda}\left(sin\alpha_i + sin\alpha_f\right) \qquad \text{(2-8)}$$

where $\overrightarrow{q_z}$ indicates out-of-plane relevant to sample surface, $\overrightarrow{q_x}$ and $\overrightarrow{q_y}$ are in-plane direction which are parallel and perpendicular to the incident beam. GIWAXS could provide crystallisation with all sets of orientation with respect to both in-plane and out-of-plane directions.

The GIWAXS measurements were carried out at the 12.3.2 microdiffraction beamline in the Advanced Light Source (ALS). A customised chamber is made for the spin-coating, anti-solvent deposition, and thermal annealing of perovskite thin film and in-situ measurements. X-ray beam with energy of 10 keV was set to 1° or 2° (depending on samples) was used. The sample detector distance (SDD) was ≈155 mm and the detector was positioned at an angle of 35° from the sample plane. The GIWAXS data were recorded with an integration time of one second using a Pilatus 1 M 2D detector (Dectris Ltd.). The measured GIWAXS frames were calibrated using an Al_2O_3 reference sample and each frame was integrated along the χ-axis from χ = −70° to χ = 70°.
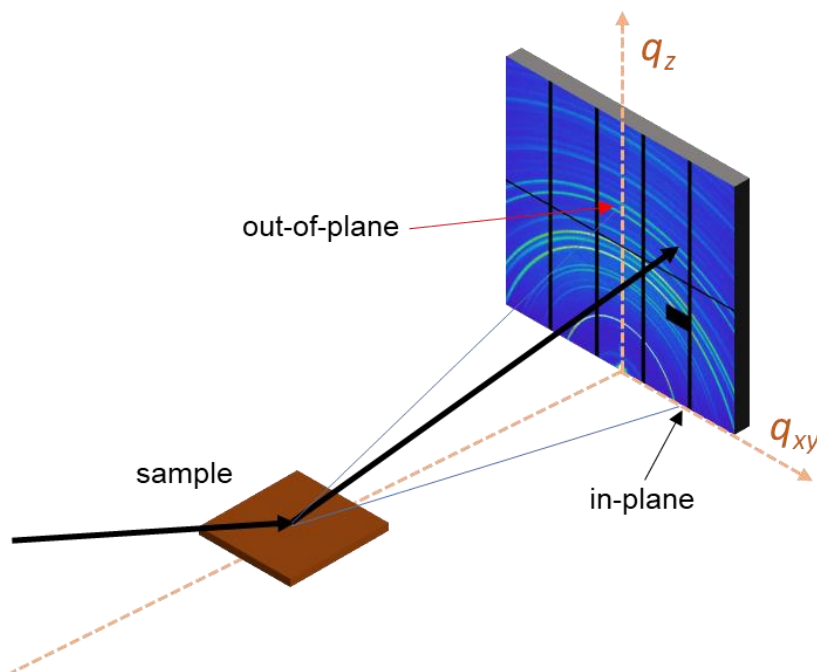
Figure 2-9: The schematic of the set-up for synchronised in-situ GIWAXS.

2.2.7. Time-resolved Photoluminescence Spectroscopy (TRPL)

The emission behaviour of perovskite film is characterised by TRPL. The perovskite semiconductors absorb photons with energy larger than the bandgap and generate charge carriers in conduction band (CB) and valence band (VB). The generated charge carriers are either collected by charge contacts (e.g. HTL and ETL) or remain stationary at perovskite film. The stationary charge carriers will recombine after a specific period of time, which is known as charge carrier lifetime. The recombination behaviour is discussed in Section 1.5.5. In the case of radiative recombination, electron-hole pair emits a photon which can be detected by photoluminescence spectroscopy (PL) and a peak will be identified in the PL spectra.

The TRPL measurement is produced by radiative recombination of photogenerated electrons and holes and is quenched when carriers are extracted[137].   For the TRPL measurements, the perovskite layers were deposited onto bare ITO substrates. PL decays were measured in a nitrogen-filled chamber with a Hamamatsu streak camera using 200 fs laser pulses at 515 nm for excitation with a pulse energy density of about 60 nJ/cm^2 and a pulse repetition rate of 200 kHz. Time-integrated PL spectra were measured with the same set-up, but the excitation was at 343 nm. The lifetime of TRPL results were estimated as the e^{-1} PL decay time.

The dynamics of the exciton density $N(x,t)$ at the distance x from the quenching surface can be described as:

$$\frac{\partial N(x,t)}{\partial t} = -kN(x,t) + D\frac{\partial^2 N(x,t)}{\partial^2 x^2} \qquad (2\text{-}9)$$

where k is the exciton rate at the bulk and D is the exciton diffusion constant. The boundary condition at the quenching interface is defined as $D\partial N(x,t)/\partial x = SN(x,t)$ at $x = 0$, where S is the surface quenching velocity. For the non-quenching surface where $x = d$ (film thickness), $\partial N(x,t) = 0$. Perovskite films have fast exciton diffusion, which corresponds to $D \gg Sd$, the gradient of the exciton density depends on x and the average exciton density is:

$$N_{av}(t) = \frac{1}{d}\int_0^d N(x,t) \qquad (2\text{-}10)$$

the average exciton density is proportional to the measurement TRPL intensity, assuming that the initial excitations are uniform since the film is optically thin, equation (2-9) can be rearranged as:

$$\frac{dN_{av}}{dt} = -kN_{av} - D\frac{SN_{av}}{d} \qquad (2\text{-}11)$$

meanwhile, exciton density in the bulk film N_b, can be described as:

$$\frac{dN_{av}}{dt} = -kN_b \qquad (2\text{-}12)$$

a new function $g(t)$ can then be solved as:

$$g(t) = \frac{N_{av}}{N_b} = \exp\left(-\frac{St}{d}\right) \qquad (2\text{-}13)$$

where $g(t)$ can be obtained by taking the ratio of the TRPL intensity measured[138]. The TRPL intensity is proportional to the product of the electron density in the conduction band n and the hole density in the valence band p. We assume p is constant, then PL ~n and diffusion equation is for electrons. In this case, by comparing $g(t)$ for perovskite layers, the electron extraction time can be obtained for the perovskites.

2.2.8. Wavelength Dispersive X-ray Spectroscopy (WDX)

WDS is a technique to identify chemical elements using characteristic X-rays. WDS identifies presence and quantities of chemical elements by detecting characteristic X-rays emitted from atoms irradiated by high-energy beam.

During the measurements, the sample is irradiated by high energy beam. When a high energy particle (e.g. electron or X-ray photon) bombard an electron in the inner shell of an atom, the energy of the particle could "knock out" an electron from inner shell from its original position in an atom. The atom could be ionised due to the ejection of the knocked-out electron. Since the ionisation is an excitation status, the atom will be returning to the original state by refilling the inner electron vacancy by an outer shell electron, The electron transition between outer shell to inner shell will lose amount of energy equals to the difference of energy levels, which accompanied by release of characteristic X-ray photons. The energy of the characteristic X-ray is well defined and dependent on the type of atom. These processes are shown in **Figure 2-10 (a)**. The emitted X-rays is then passing through a collimator to be aligned and directed to an analyser crystal, also known as diffracting crystal, to be diffracted. The rotating X-ray photon counter finally collects the diffracted beam from analyser crystal and scans a range of 2 to detect specific wavelengths of characteristic X-ray from the sample. The WDS experimental set-up are shown in **Figure 2-10 (b)**.

The WDS system can detect relative wavelengths variation ($\Delta\lambda/\lambda$) in the range of 0.002-0.02, which corresponds to energy range of 0.01-0.1 keV. The resolution is about one order of magnitude higher than that of EDS.

In this thesis, WDX spectra were acquired using a JEOL JXA-8530F electron probe microanalyser (EPMA). An 8 keV, 100 nA beam was widely defocused to a 50 µm spot diameter. C K_α, Br L_α, I L_α and Cl K_α X-rays were measured using LDE2, TAP, PET and PET crystals respectively. The WDX experiment was carried out by Dr. Paul Edwards from the University of Strathclyde.
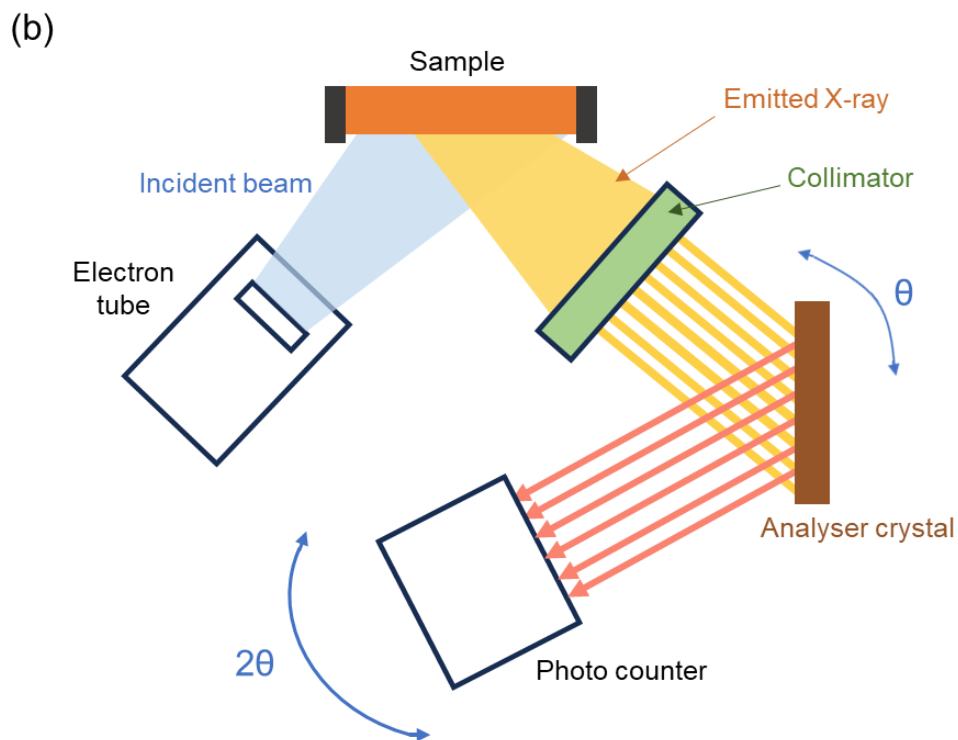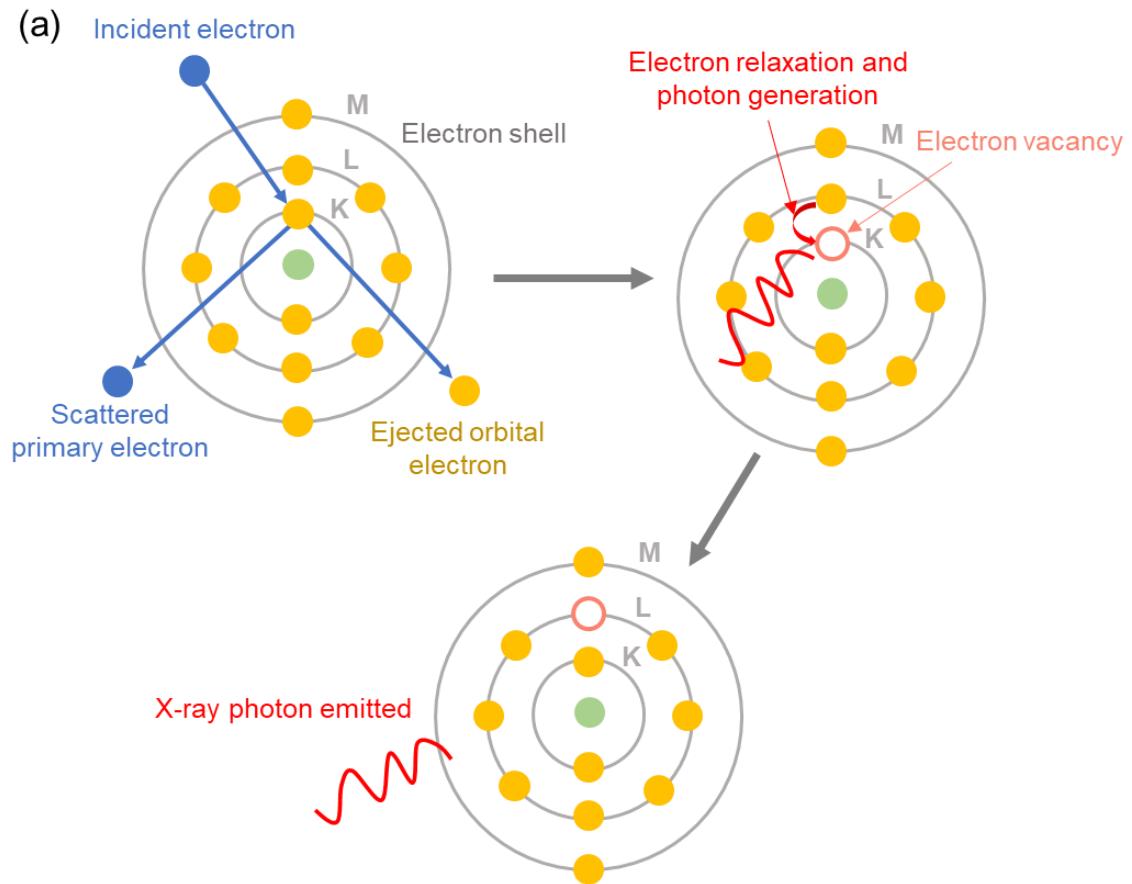
Figure 2-10: (a) Illustration of working processes of wavelength dispersive X-ray spectroscopy. (b) Schematic of WDS experimental set-up.

2.2.9. Cathodoluminescence (CL)

CL is a well-established characterisation to understand the optoelectronic properties of perovskite thin films including impurity or defect energy levels, dopant concentrations, charge carrier lifetimes or variations in composition[139,140]. CL refers to the light emission from a material under excitation stimulated by a high energy electron beam (or "cathode ray").

The luminescence behaviour from CL is induced by high energy electron beam. During the measurement, the sample is hit by an electron beam. While traveling with in the material, electrons quickly lose energy via impact ionisation, generating hole-electron pairs. The excited charge carriers experience drift or diffusion process and result in radiative or non-radiative recombination, leading to luminescence. The advantage of CL method is that the injection can be confined within a substantially sub-μm-scale, this enables the spatial resolution of the measurement to surpass the diffraction limit of optical PL methods.

In this thesis, CL measurements were carried out in a modified FEI Sirion 200 (FEI Company, Hillsboro, OR, USA) field emission gun SEM at room temperature in the University of Strathclyde by Dr. Paul Edwards.
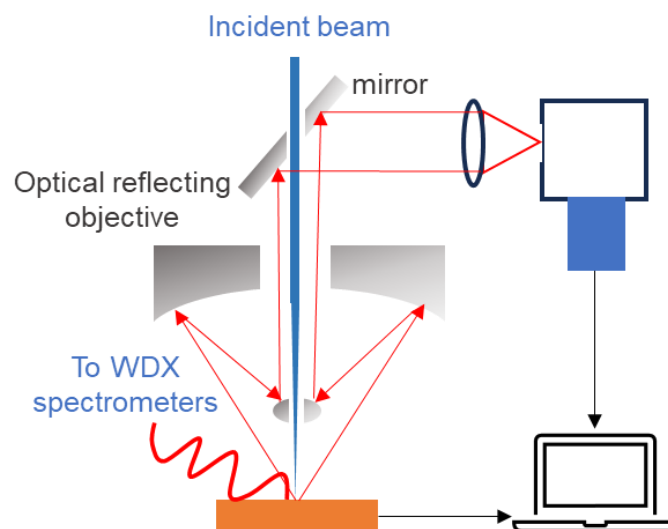

Figure 2-11: Schematic of cathodoluminescence experimental set-up.

2.3. Optoelectronic characterisation

2.3.1. Device Performance Current-Voltage (*J-V*) Measurement

Before the measurement, the light intensity needs to be calibrated for both 1 sun and indoor measurement to ensure the light intensity is at the standard level to obtain reliable measurement results.

1 sun calibration is done by a Newport calibrated reference cell system. The system is consisting of a readout device and a 2×2 cm calibration monocrystalline solar cell, covered by a fused silica window. During the calibration, the monocrystalline solar cell is illuminated by the light of solar simulator and the readout device reads the solar simulator irradiance in sun units.
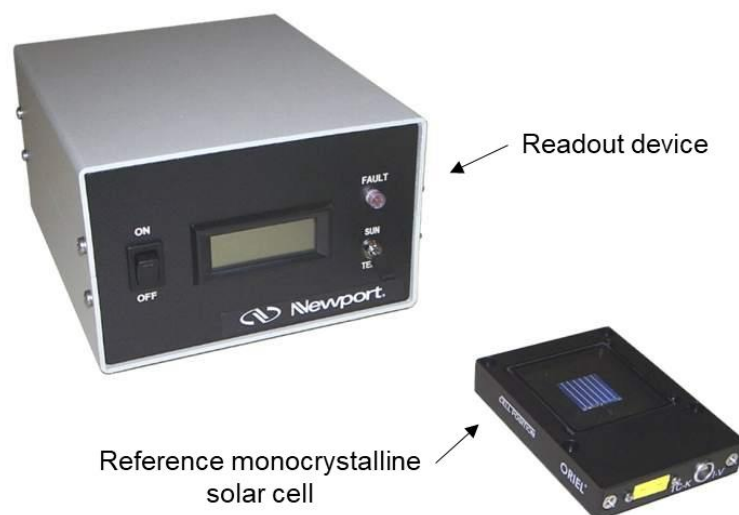
Indoor calibration is done by an ILT960-UV spectroradiometer. ILT960-UV is used to measure both the light's amplitude and wavelength and provide calibrated spectral irradiance and power measurements. It consists of a right angle cosine adapter to detect light, an optic fibre to direct the light to the spectrometer, and the spectrometer itself to analyse the irradiance and illumination level.

For current-voltage characteristics, 1 sun measurement was carried out using a solar simulator with Xenon Arc lamp (150 W, 50 × 50 mm, Class AAA, Sciencetech Solar

simulator) at the light intensity of 100 mW/cm^2 (AM 1.5G). The indoor illumination measurements were carried out using a "warm white" LED bulb with colour temperature 2700 K. The intensity of the warm white LED was fixed to 0.3 mW/cm^2, corresponding to 1000 lux. The current-voltage characterisation was measured with Ossila Source Measure Unit (SMU) and an Ossila Solar Cell IV software. The devices were masked by a metal mask with an aperture of 0.05 cm^2 to define the active area of photovoltaic cell. The devices are measured under a bias scan of -0.1 V to 1.2 V range (forward scan), followed by a reverse scan of 1.2 V and -0.1 V, with a voltage setting time of 0.2 s. The voltage increment of *J-V* characteristic was 0.05 V and the scan rates was 0.2 V/s. For the maximum power point tracking (MPPT) 5 measurement, the devices were characterized under the same conditions for *J-V* characteristics and were hold under the maximum power point condition for 3 or 5 minutes to obtain the MPPT PCE curve.

2.3.2. External Quantum Efficiency (EQE)

EQE quantifies the ratio of the number of electrons coming out of the device to the external circuit and the number of photons incident. It provides great representation of photocurrent of PV module by measuring the effect of the optical properties of the device. EQE is a wavelength dependent technique and measured by illuminating the solar cell with monochromatic light of wavelength and measuring the photocurrent. The external quantum efficiency is determined as:

$$EQE(\lambda) = \frac{I_{ph}(\lambda)}{q\Psi_{ph,\lambda}} \qquad (2\text{-}14)$$

where q is the elementary charge and $\Psi_{ph,\lambda}$ is the spectral photon flow incident on the solar cell. The photon flow is usually determined by measuring the EQE of a calibration photo diode under the same light source. Hence, the calculation of EQE is done by:

$$EQE(solar\ cell) = \frac{EQE(photo\ diode) \times I_{ph}(solar\ cell)}{I_{ph}(photo\ diode)} \qquad (2\text{-}15)$$

The EQE measurements were carried out at zero bias by using a monochromatic light, which was obtained by attaching the dual-grating monochromator to a xenon arc lamp. A silicon photodiode made by National Physical Laboratory was used to calibrate the incident photons at each wavelength. The number of incident photons was calculated

for each wavelength by using a National Physical Laboratory calibrated silicon photodiode.
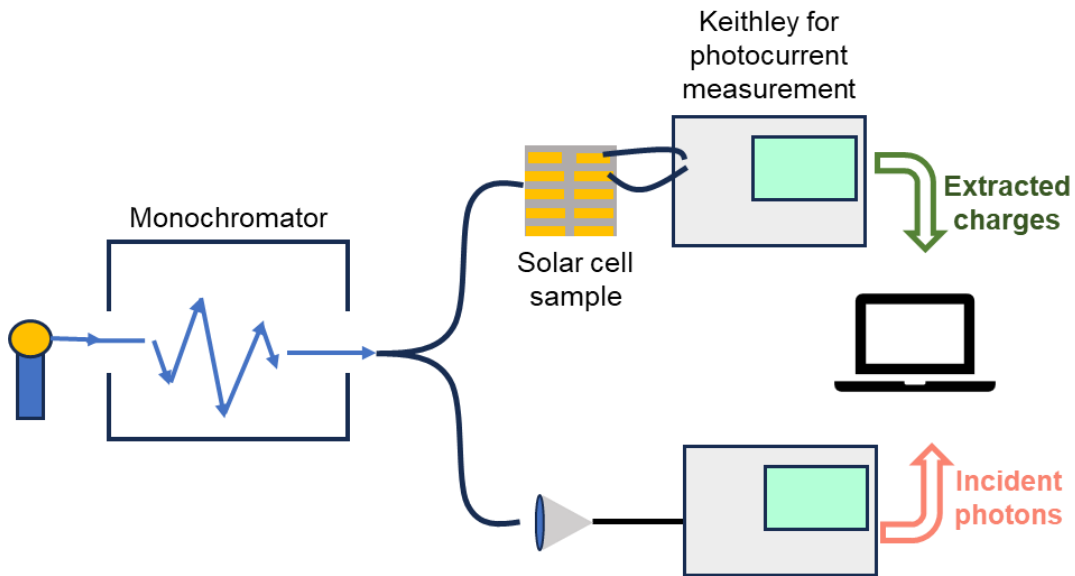
Figure 2-12: Schematic of external quantum efficiency experimental set-up.

2.3.3. Light intensity dependent measurements

The detailed principle of light intensity dependent measurements is introduced in Section 1.4.2. Light intensity dependent measurement is used to present the charge accumulation and trap-assisted recombination level. The *J-V* measurements are carried out by illuminating the devices under solar simulator and Fluxim Paios platform under various levels of light intensity. The light intensity is varied from 0.1% of 1 sun to 100% of 1 sun and is adjusted by tuning the aperture of light source.
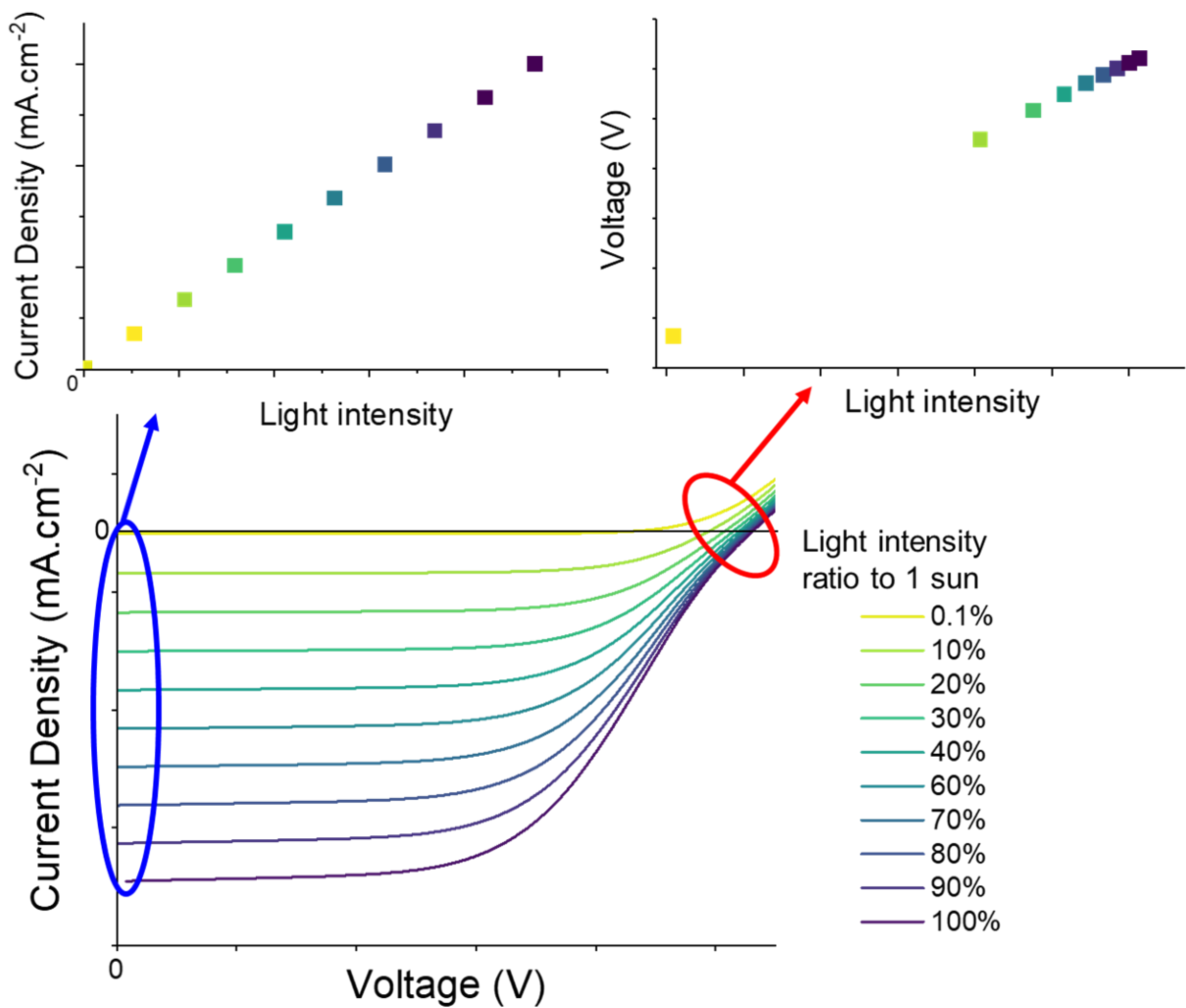
Figure 2-13: Illustration of how the photovoltaic parameters with varied light intensity are extracted in light intensity dependent measurements.

2.3.4. Transient Photovoltage (TPV) measurement

TPV is a time-resolved characterisation to study charge carrier dynamics by probing their carrier recombination processes. This measurement is based on V_{OC} perturbation induced by a transient light pulse, which can be correlated to small perturbation of quasi-Fermi level[141].

Based on the definition of V_{OC}, the V_{OC} can be described by the quasi-Fermi level splitting:

$$V_{OC} = \frac{1}{q}(E_{FN} - E_{FP}) \qquad (2\text{-}16)$$

It can be rearranged by considering the bandgap and charge carrier concentrations:

$$V_{OC} = \frac{E_g}{q} - \frac{k_B T}{q} \ln \left(\frac{N_c N_v}{n.p} \right) \qquad (2\text{-}17)$$

where n is the electron concentration and p is the hole concentration. N_c and N_v are the corresponding effective density of states. By the taking the derivative of the equation (2-14) as a function of time, it can be rearranged by:

$$\frac{dV_{OC}}{dt} = - \frac{k_B T}{q} \left(\frac{1}{\tau_n} + \frac{1}{\tau_p} \right) \qquad (2\text{-}18)$$

$$\frac{dV_{OC}}{dt} = - \frac{k_B T}{q} \left(\tau_{eff} \right)^{-1} \qquad (2\text{-}19)$$

where τ_n is the electron lifetime and τ_p is the electron lifetime. τ_{eff} is the effective lifetime measured by transient decay of V_{OC} combining of both electron and hole lifetimes in TPV measurement.

To carry out TPV measurements, the solar cell device is firstly illuminated continuously by a background light to generate a stabilised background V_{OC}. The solar cell device is kept under open circuit condition so that no current flow exist within the device. After the V_{OC} is stabilised, a short-lived light pulse within micro-second scale is applied to excite additional perturbation of voltage by induce an additional perturbation of quasi-Fermi level. The variation of the V_{OC} (ΔV) is proportional to the photo-generated carriers by the laser pulse. As the solar cell is in open-circuit, after the light pulse is withdrawn, the "extra" photo-generated carriers are forced to recombine, which leads to the decay of the transient to the initial V_{OC}. The transient lifetime is hence measured. A schematic illustration of TPV measurement is shown in **Figure 2.14**. The relationship of measured carrier lifetime and V_{OC} can be described by the following equation[142]:

$$\tau = \tau_0 e^{-\beta V_{OC}} \qquad (2\text{-}20)$$
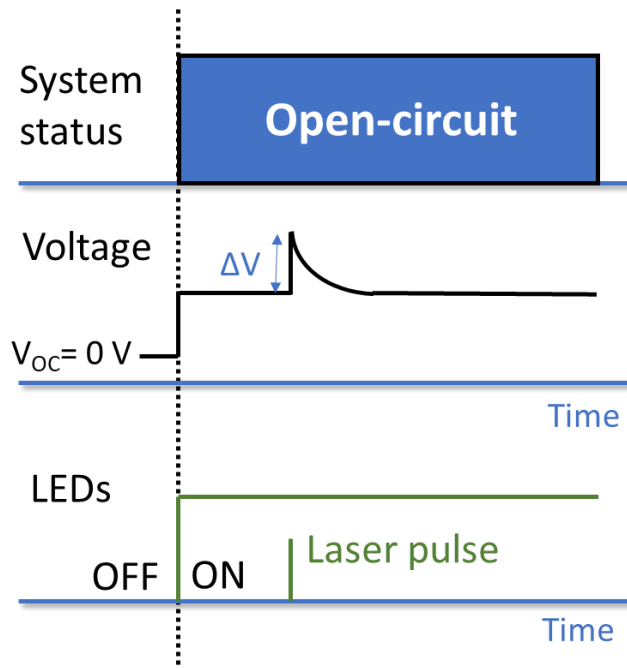
Figure 2-14: Representation of the TPV signal.

2.3.5. Transient Photocurrent (TPC) measurement

TPC is a measurement to quantify the charge extraction of solar cells. The solar cell device is firstly illuminated under the same conditions as TPV measurements, after the V_{OC} is stabilised, the device is turned to short-circuit condition and the charge carrier density is calculated by integrating the decay of photocurrent. The total charge (Q) can be calculated by the following equation:

$$Q = \int_{t=0}^{t=t} I(t)dt \qquad (2\text{-}21)$$

and the capacitance can be calculated as:

$$C = \frac{\Delta Q}{\Delta V_0} \qquad (2\text{-}22)$$

where ΔV_0 is the voltage variation at different background intensities. The steady state carrier density can be calculated by integrating C with respect to voltage.

$$n = \frac{1}{Aed} \int_0^{V_{OC}} CdV \qquad (2\text{-}23)$$

where A is the device area, e is the charge of electron, d is the thickness of the perovskite layer. Finally, the relationship of charge carrier density and light bias (corresponding V_{OC}) can be described as:

$$n = n_0 \exp(\gamma V_{OC}) \qquad (2\text{-}24)$$
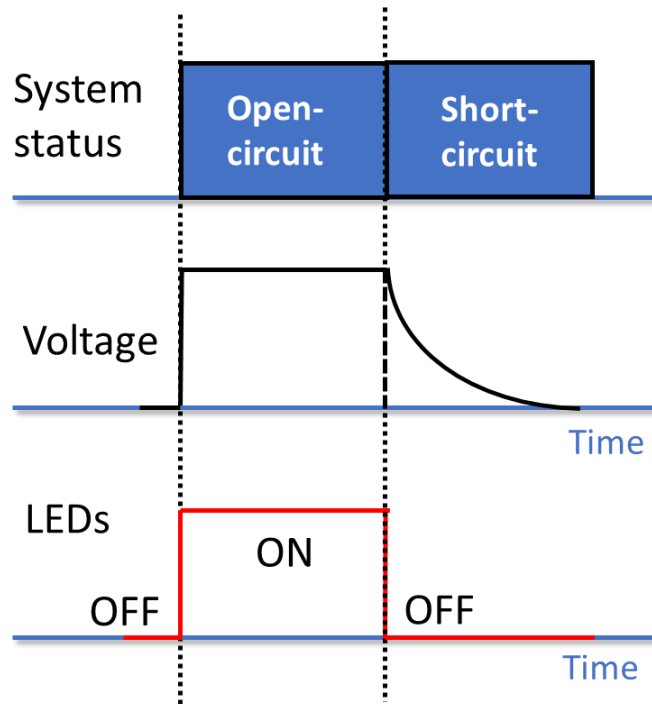
Figure 2-15: Representation of the TPC signal.

2.3.6. Space-Charge Limited Current (SCLC) measurement

SCLC is the characterisation to evaluate the trap density and charge carrier mobility of semiconductors by measuring the current-voltage response of single carrier devices. Perovskite layer is sandwiched between HTL or ETL on both sides so that only holes or electrons can be injected by the alignment of conduction, or valence band. A schematic of single carrier device with symmetric ohmic contacts on both side is shown in **Figure 2-16**[143]. The Ohmic contact results in a space charge region where charges are accumulated. The width of space charge region can be described by following equation (2-25):

$$\lambda = \frac{\pi}{2}\left(\frac{2kTK\epsilon_0}{e^2 N_t}\right)^{1/2} \exp\left(\frac{\psi_1 - \chi - E_t}{2kT}\right) \qquad (2\text{-}25)$$

where K is the dielectric constant, N_t is the defect density. Hence, it can be noticed that the width of space charge region is dependent on the dielectric constant and inversely to the trap states. The measurement of SCLC is carried out by sustaining the space charge region to the full width of semiconductor layer by applying voltage bias to the devices, in which condition that the traps are filled by the applied voltage. In this case, all the additional injected charge carriers can move freely without influences from traps and the mobility of charge carriers is completely dependent on the property of target material for the measurement. Hence, the SCLC can be a powerful tool to investigate both the defect states of the semiconductor and the charge carrier mobility.

During the measurement, the *J-V* curve can be divided into several stages. Firstly, the low-voltage regime follows Ohm's law, in which the slope $\frac{dlog(J)}{dlog(V)}$ of 1. This Ohmic region is followed by a trap filling region with slope higher than 2. When the applied voltage is higher than the trap filling voltage (the point where all the traps are filled by injected carriers), a SCLC, or Child's region is then achieved in high voltage regime, which follows the Mott-Gurney law[144].

$$J_{SCLC} = \frac{9}{8}\varepsilon_0\varepsilon_n\mu\frac{V^2}{L^3} \quad (2\text{-}26)$$

where *V* is the applied voltage, *L* is the thickness of active layer. ε_0 is the permittivity of free space, ε_n is the dielectric constant. In this case, by fitting the Child's region, the charge carrier mobility *μ* can be calculated.
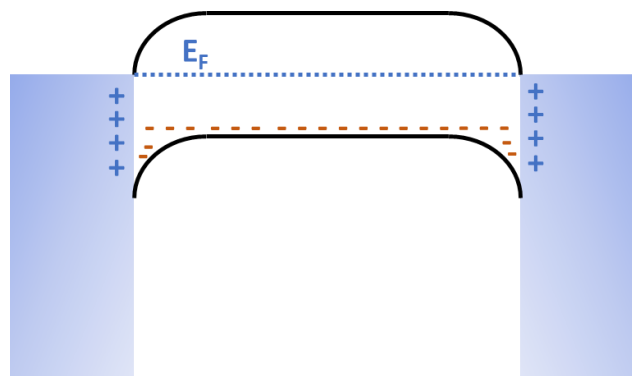

Figure 2-16: Schematic illustration of SCLC measurement.

2.3.7. Dark current measurement

When the layers in perovskite solar cell device is contacted, a potential difference exists at the junction. This potential difference initiates an opposite current flow compared to the photocurrent, which reduces the output current from the short circuit status. This reverse current is usually called dark current. The dark current can be present by the following equation in terms of its definition[145]:

$$J_{inj} = AT^2 \exp\left(-\frac{q\Phi_{inj}}{k_B T}\right) \quad (2\text{-}27)$$

where Φ_{inj} is the work function difference between electrode and the transport layer, e.g. work function difference between ITO and LUMO level of Poly-TPD for electron injection. The dark current is mainly contributed by the injected minority carrier through defect states hence dark current is a crucial measurement of defect density within devices especially transport layers[146]. Dark current measurements were carried out with a characterization platform, Paios, Fluxim AG, Switzerland.

2.3.8. Impedance spectroscopy

Impedance spectroscopy is a technique to understand the charge carrier dynamics of solar cells. It is an ample set of light and voltage perturbation methods in the time domain that measure the recovery toward the equilibrium state. The impedance of device is measured at several frequencies by applying a small sinusoidal voltage and measure the current in the frequency domain. Different device physical effects can be understood by using a large range of frequencies. The small sinusoidal voltage is applied to the solar cell device following:

$$V(t) = V_0 + V_{amp} \sin(\omega t) \quad (2\text{-}28)$$

where V_0 is the offset voltage, V_{amp} is the voltage amplitude and ω is the angular frequency. In terms of the applied voltage, the current response can be expressed as:

$$I(t) = I_{amp} \sin(\omega t + \phi) = I_{amp} e^{i(\omega t + \phi)} \quad (2\text{-}29)$$

The signal of voltage and current are described in **Figure 2-17 (a)**. Impedance spectroscopy is performed at various frequencies under different offset voltages or illumination levels. The complex impedance Z can be calculated according to:

$$Z(t) = \frac{V(t)}{I(t)} = Z_{amp}e^{-i\phi} \qquad (2\text{-}29)$$

For the analysis of impedance, the impedance Z is usually represented by resistance and reactance as shown in **Figure 2-17 (b)**.
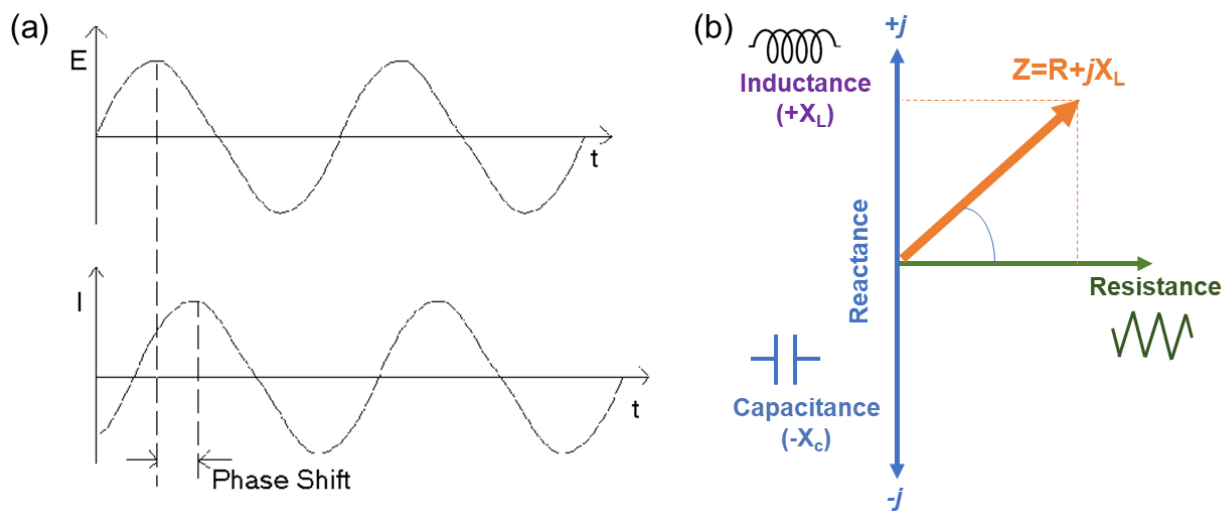
Figure 2-17: (a) Illustration of impedance voltage perturbation signal and current response. (b) Illustration of impedance $Z=R\text{-}jX$.

Chapter 7

Conclusion and Outlook

7.1. Summary

In this thesis, the performance of indoor photovoltaic devices and corresponding device physics are investigated from the perspectives of device architectures, hysteresis behaviour, transport layer types and perovskite active layer properties. We understand that developing efficient indoor PV starts with an understanding of the difference between indoor artificial light sources and outdoor sunlight. These light sources differ in their spectra and illumination intensities, which emphasise the importance of reducing defects and widening bandgap of perovskites to fit with indoor illumination spectra. The comparison between n-*i*-p and p-*i*-n device architecture indicates that interfacial defects play crucial role in determining the indoor photovoltaic

performance. Particular attention should be paid to hysteresis behaviour as we found that the hysteresis is strengthened under low intensity indoor lighting conditions due to severer trapping/de-trapping. This is the first study targeting on hysteresis behaviour of indoor photovoltaic devices, which could provide significant guideline regarding the understanding of hysteresis. By revealing the detrimental effect of employing metal oxide hole transport layers, an interlayer passivation method with 2PACz self-assembled monolayer is developed to passivate the defects, which proves to effectively improve the performances by improving the morphology, suppressing leakage current and light soaking effect, and improving the charge mobility. The study targeting on wider bandgap perovskite indoor photovoltaics revealed that to keep the Cl in the triple anion perovskite and to reap the beneficial effects of high V_{OC} and enhanced charge carrier lifetime, the thermal annealing duration should be carefully optimised. Detailed microstructural and optoelectronic investigations of the triple anion perovskite revealed its excellent crystalline quality, widened bandgap, lower density of trap states and longer carrier lifetime, all contributing positively to the enhanced photovoltaic properties.

7.1.1. Device Architecture

The photovoltaic behaviour and device physics of n-*i*-p and p-*i*-n devices are compared under indoor lighting conditions in Chapter 3. It is shown that n-*i*-p devices exhibited lower PCE and suffered from higher hysteresis, this is attributed to higher trap-assisted recombination, ion migration of active layer and poor charge extraction efficiency as pointed from light intensity dependent measurements of V_{OC} and FF. Considering the existence of hysteresis, it is also vital to notice that compared to *J-V* characterisation, which is rather a transient technique, the maximum power point tracking method should be prioritised to assess the real performance of halide perovskite indoor solar cell devices.

7.1.2. Transport Layer Properties and Interfaces

The charge transport layers play vital role in determining the device performance and stability. Among the wide range of charge transport materials, the layer should be carefully selected considering various factors including the band alignment, charge mobility, wettability and preparation conditions. In chapter 4, Spiro-OMeTAD shows

promising performance as hole transport layer in n-*i*-p devices although additional doping is required to obtain appropriate energy level and hole mobility of Spiro-OMeTAD. For p-*i*-n devices, metal oxide HTMs commonly exhibit lower performance due to higher interlayer and bulk defects, with further concern of light soaking effect. Positively, 2PACz is proved to be an efficient passivation layer by providing better coverage and improved morphology. Until now, the superiority of 2PACz as a promising interlayer has been gradually realised by the research community. 2PACz, in addition to its functional group modified variations have been implemented into top level research as passivation layers and achieved promising results[147–150]. It is expected that utilising 2PACz appropriately could be a promising method to boost the performance of perovskite solar cell devices.

7.1.3. Wide-bandgap Perovskite for Indoor Photovoltaics

To fit with indoor illumination spectrum which only has visible spectral range, wide-bandgap perovskites is required to boost V_{OC} by reducing thermalisation loss. Triple anion perovskite discussed in Chapter 5 has a bandgap of 1.68 eV, which provides improved crystallinity, TRPL lifetime (indicating less trap-assisted recombination) for thin films. The triple anion perovskite-based device provides high performance over 26% and extraordinary optoelectronic properties including reduced defects and improved charge carrier lifetime. It provides a promising route for wide-bandgap indoor photovoltaic development by varying halide site with Br and Cl to obtain highly efficient devices.

7.2. Outlook

During the study of this PhD thesis, concerns are also identified which needs to be addressed in future work. Firstly, wide-bandgap perovskites are required to fit with indoor spectral range, but the fast crystallisation of wide-bandgap perovskites results in relatively poor film quality with high defect density, especially for bandgap larger than 1.75 eV. In addition to the $MAPbI_{2.6}(BrCl)_{0.2}$ triple anion composition discussed in Chapter 5, we have synthesised additional triple anion perovskite with higher ratio of Br and Cl, which is shown in **Figure 7-1 (a)**, the corresponding bandgap of each composition is shown in **Figure 7-1 (b)**. Noticeably, the bandgap of triple anion

perovskite can be widen to maximum 1.85 eV with composition MAPb(IBrCl). However, from the sample picture in Figure 7-1 (b), the quality of thin film of 1.76 eV is already poor and not suitable for photovoltaic applications. This is due to the fast crystallisation kinetics and poor solubility of precursors, i.e. MACl in DMF, result in discontinuous coverage and irregular morphology, indicating large defect density[88,151]. A promising method to suppress the fast crystallisation of wide-bandgap perovskite is by manipulating annealing atmospheres with essential components, e.g. excess MACl vapour assisted-annealing to compensate the low solubility of MACl[152].
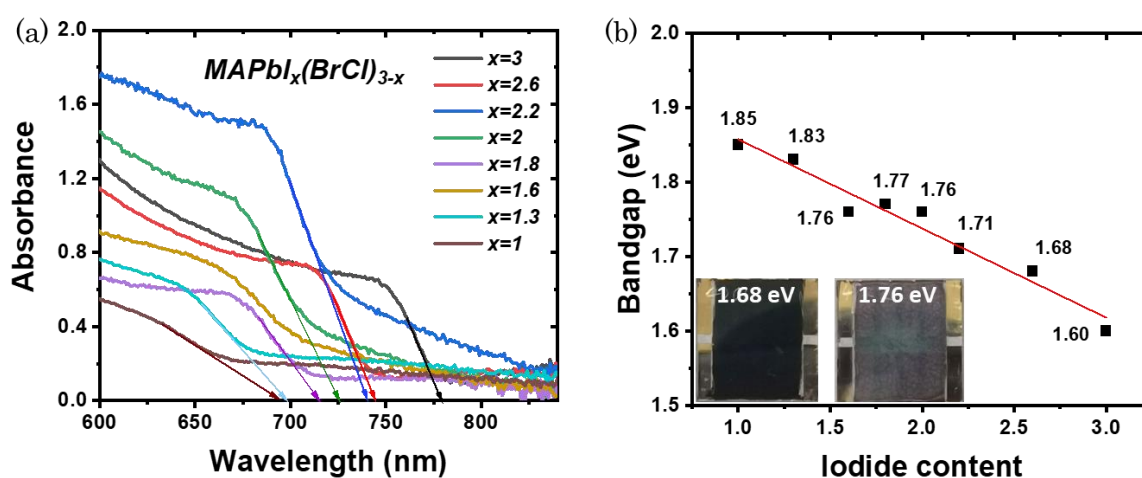

Figure 7-1 (a) Absorbance spectra of triple anion $CH_3NH_3PbI_X(BrCl)_{3-X}$ perovskite film from UV-Vis spectroscopy. (b) Corresponding bandgap from the UV-Vis spectra of Figure 7-1 (a). Inset: image of 1.68 eV and 1.76 eV triple anion perovskite film based solar cell devices.

Secondly, wide-bandgap perovskite based photovoltaic devices usually suffer from severe non-radiative energy loss, which means the experimental photovoltaic parameters are significantly lower than the theoretical calculations, especially for an open-circuit voltage (V_{OC}) loss of 0.4-0.5 V. The reason for the energy losses is now primarily attributed to thermalization loss, junction loss and non-radiative recombination loss. One of the most significant origins of energy loss is the energy misalignment by employing wide-bandgap perovskite. When the activelayer is replaced by wide-bandgap perovskites, the band alignment designed for charge transport layers and regular bandgap perovskite is misaligned, which results in dramatic charge accumulation at interfaces, causing significant non-radiative recombination loss. A promising method is to introduce charge-blocking interlayers

between perovskite and transport layer to reduce the concentration of specific carriers to suppress the non-radiative recombination and also contributing to tune the work function/valence band accordingly.

Despite these concerns, this thesis has extended and developed new knowledge on behaviours of indoor photovoltaic devices. *J-V* hysteresis of halide perovskite indoor PV is important in designing efficient p-*i*-n and n-*i*-p device and active and transport layers, which emphasises that the device architectures should be carefully selected, and attention should be paid to suppress ion migration. The importance of transport layer selection is also emphasised, the selection of transport layers should achieve ideal energy alignment, charge carrier mobility and lifetime, and suppressed leakage. Wide-bandgap perovskites should be employed to fit with indoor spectral range to reduce thermalisation and improve photovoltaic performances. These aspects provide guidance for developing more efficient and reliable indoor perovskite photovoltaic devices and employing them to power microelectronic components to achieve the vision of IoT.

Bibliography

1. Wilson, G. M. *et al.* The 2020 photovoltaic technologies roadmap. *Journal of Physics D: Applied Physics* vol. 53 Preprint at https://doi.org/10.1088/1361-6463/ab9c6a (2020).

2. Nelson, J. *The Physics of Solar Cells*. (PUBLISHED BY IMPERIAL COLLEGE PRESS AND DISTRIBUTED BY WORLD SCIENTIFIC PUBLISHING CO., 2003). doi:10.1142/p276.

3. Ramasamy, V. *et al. U.S. Solar Photovoltaic System and Energy Storage Cost Benchmarks, With Minimum Sustainable Price Analysis: Q1 2023*. www.nrel.gov/publications. (2050).

4. Richter, A. *et al.* Design rules for high-efficiency both-sides-contacted silicon solar cells with balanced charge carrier transport and recombination losses. *Nat Energy* **6**, 429–438 (2021).

5. Reese, M. O. *et al.* Increasing markets and decreasing package weight for high-specific-power photovoltaics. *Nat Energy* **3**, 1002–1012 (2018).

6. Scarpulla, M. A. *et al.* CdTe-based thin film photovoltaics: Recent advances, current challenges and future prospects. *Solar Energy Materials and Solar Cells* vol. 255 Preprint at https://doi.org/10.1016/j.solmat.2023.112289 (2023).

7. Ballif, C., Haug, F. J., Boccard, M., Verlinden, P. J. & Hahn, G. Status and perspectives of crystalline silicon photovoltaics in research and industry. *Nature Reviews Materials* vol. 7 597–616 Preprint at https://doi.org/10.1038/s41578-022-00423-2 (2022).

8. Wehrenfennig, C., Eperon, G. E., Johnston, M. B., Snaith, H. J. & Herz, L. M. High charge carrier mobilities and lifetimes in organolead trihalide perovskites. *Advanced Materials* **26**, 1584–1589 (2014).

9. Steirer, K. X. *et al.* Defect Tolerance in Methylammonium Lead Triiodide Perovskite. *ACS Energy Lett* **1**, 360–366 (2016).

10. Jeon, N. J. *et al.* Compositional engineering of perovskite materials for high-performance solar cells. *Nature* **517**, 476–480 (2015).

11. Best Research-Cell Efficiency Chart | Photovoltaic Research | NREL. https://www.nrel.gov/pv/cell-efficiency.html.

12. Kojima, A., Teshima, K., Shirai, Y. & Miyasaka, T. Organometal halide perovskites as visible-light sensitizers for photovoltaic cells. *J Am Chem Soc* **131**, 6050–6051 (2009).

13. Lee, M. M., Teuscher, J., Miyasaka, T., Murakami, T. N. & Snaith, H. J. Efficient hybrid solar cells based on meso-superstructured organometal halide perovskites. *Science (1979)* **338**, 643–647 (2012).

14. Kim, H. S. *et al.* Lead iodide perovskite sensitized all-solid-state submicron thin film mesoscopic solar cell with efficiency exceeding 9%. *Sci Rep* **2**, (2012).

15. Jeon, N. J. *et al.* Compositional engineering of perovskite materials for high-performance solar cells. *Nature* **517**, 476–480 (2015).

16. Zhao, P., Kim, B. J. & Jung, H. S. Passivation in perovskite solar cells: A review. *Materials Today Energy* vol. 7 267–286 Preprint at https://doi.org/10.1016/j.mtener.2018.01.004 (2018).

17. Dos Santos, J. M., Jagadamma, L. K., Cariello, M., Samuel, I. D. W. & Cooke, G. A BODIPY small molecule as hole transporting material for efficient perovskite solar cells. *Sustain Energy Fuels* **6**, 4322–4330 (2022).

18. Park, J. *et al.* Controlled growth of perovskite layers with volatile alkylammonium chlorides. *Nature* **616**, 724–730 (2023).

19. Jena, A. K., Kulkarni, A. & Miyasaka, T. Halide Perovskite Photovoltaics: Background, Status, and Future Prospects. *Chem Rev* **119**, 3036–3103 (2019).

20. Jagadamma, L. K. & Wang, S. Wide-Bandgap Halide Perovskites for Indoor Photovoltaics. *Front Chem* **9**, 1–8 (2021).

21. Mathews, I., Kantareddy, S. N., Buonassisi, T. & Peters, I. M. Technology and Market Perspective for Indoor Photovoltaic Cells. *Joule* **3**, 1415–1426 (2019).

22. Sensors, L. S. I. *et al.* Perovskite PV-powered RFID : enabling low- cost self-powered IoT sensors. (2020).

23. Jagadamma, L. K., Blaszczyk, O., Sajjad, M. T., Ruseckas, A. & Samuel, I. D. W. Efficient indoor p-i-n hybrid perovskite solar cells using low temperature solution processed NiO as hole extraction layers. *Solar Energy Materials and Solar Cells* **201**, 110071 (2019).

24. Kansal, A., Hsu, J., Zahedi, S. & Srivastava, M. B. Power Management in Energy Harvesting Sensor Networks. *ACM Transactions on Embedded Computing Systems* **6**, 32 (2007).

25. Biswas, S. & Kim, H. Solar cells for indoor applications: Progress and development. *Polymers (Basel)* **12**, 1338 (2020).

26. Li, M., Igbari, F., Wang, Z. K. & Liao, L. S. Indoor Thin-Film Photovoltaics: Progress and Challenges. *Advanced Energy Materials* vol. 10 Preprint at https://doi.org/10.1002/aenm.202000641 (2020).

27. Chen, F. C. Emerging Organic and Organic/Inorganic Hybrid Photovoltaic Devices for Specialty Applications: Low-Level-Lighting Energy Conversion and Biomedical Treatment. *Advanced Optical Materials* vol. 7 Preprint at https://doi.org/10.1002/adom.201800662 (2019).

28. Kim, J. *et al.* Chlorine Incorporation in Perovskite Solar Cells for Indoor Light Applications. *Cell Rep Phys Sci* **1**, 100273 (2020).

29. Müller, M. F., Freunek, M. & Reindl, L. M. Maximum efficiencies of indoor photovoltaic devices. *IEEE J Photovolt* **3**, 59–64 (2013).

30. Cheng, R. *et al.* Tailoring Triple-Anion Perovskite Material for Indoor Light Harvesting with Restrained Halide Segregation and Record High Efficiency Beyond 36%. *Adv Energy Mater* **9**, (2019).

31. Zhang, L., Zhang, J. & Yu, J. S-scheme photocatalyst. in *Interface Science and Technology* vol. 35 53–102 (Elsevier B.V., 2023).

32. Kahn, A. Fermi level, work function and vacuum level. *Materials Horizons* vol. 3 7–10 Preprint at https://doi.org/10.1039/c5mh00160a (2016).

33. Cahen, D. & Kahn, A. Electron energetics at surfaces and interfaces: Concepts and experiments. *Advanced Materials* **15**, 271–277 (2003).

34. Mead, C. A. & Spitzer, W. G. Fermi Level Position at Semiconductor Surfaces. *Phys Rev Lett* **10**, 471–472 (1963).

35. Goo, J. S., Shin, S. C., You, Y. J. & Shim, J. W. Polymer surface modification to optimize inverted organic photovoltaic devices under indoor light conditions. *Solar Energy Materials and Solar Cells* **184**, 31–37 (2018).

36. Kippelen, B. & Brédas, J. L. Organic photovoltaics. *Energy Environ Sci* **2**, 251–261 (2009).

37. Gray, J. L. The Physics of the Solar Cell. in *Handbook of Photovoltaic Science and Engineering* 61–112 (John Wiley & Sons, Ltd, Chichester, UK, 2005). doi:10.1002/0470014008.ch3.

38. Chem, J. M., Qi, B. & Wang, J. Open-circuit voltage in organic solar cells. 24315–24325 (2012) doi:10.1039/c2jm33719c.

39. Courtier, N. E. Interpreting ideality factors for planar perovskite solar cells: Ectypal diode theory for steady-state operation. *Phys Rev Appl* **14**, 1 (2020).

40. Thongprong, N., Supasai, T., Li, Y., Tang, I. M. & Rujisamphan, N. Insights into Recombination Processes from Light Intensity–Dependent Open-Circuit Voltages and Ideality Factors in Planar Perovskite Solar Cells. *Energy Technology* **8**, 1–9 (2020).

41. Koster, L. J. A., Mihailetchi, V. D., Ramaker, R. & Blom, P. W. M. Light intensity dependence of open-circuit voltage of polymer:fullerene solar cells. *Appl Phys Lett* **86**, 1–3 (2005).

42. Neukom, M., Züfle, S., Jenatsch, S. & Ruhstaller, B. Opto-electronic characterization of third-generation solar cells. *Sci Technol Adv Mater* **19**, 291–316 (2018).

43. Green, M. A. Solar cell fill factors: General graph and empirical expressions. *Solid State Electron* **24**, 788–789 (1981).

44. Steim, R. *et al.* Solar Energy Materials & Solar Cells Organic photovoltaics for low light applications. *Solar Energy Materials and Solar Cells* **95**, 3256–3261 (2011).

45. Shockley, W. & Queisser, H. J. Detailed balance limit of efficiency of p-n junction solar cells. *J Appl Phys* **32**, 510–519 (1961).

46. Ho, J. K. W., Yin, H. & So, S. K. From 33% to 57%-An elevated potential of efficiency limit for indoor photovoltaics. *J Mater Chem A Mater* **8**, 1717–1723 (2020).

47. Guillemoles, J. F., Kirchartz, T., Cahen, D. & Rau, U. Guide for the perplexed to the Shockley–Queisser model for solar cells. *Nat Photonics* **13**, 501–505 (2019).

48. Müller, M. F., Freunek, M. & Reindl, L. M. Maximum efficiencies of indoor photovoltaic devices. *IEEE J Photovolt* **3**, 59–64 (2013).

49. Ehrler, B. *et al.* Photovoltaics reaching for the shockley-queisser limit. *ACS Energy Lett* **5**, 3029–3033 (2020).

50. Guillemoles, J. F., Kirchartz, T., Cahen, D. & Rau, U. Guide for the perplexed to the Shockley–Queisser model for solar cells. *Nat Photonics* **13**, 501–505 (2019).

51. Jena, A. K., Kulkarni, A. & Miyasaka, T. Halide Perovskite Photovoltaics: Background, Status, and Future Prospects. *Chem Rev* **119**, 3036–3103 (2019).

52.   Shaikh, J. S. *et al.* Perovskite solar cells: In pursuit of efficiency and stability. *Mater Des* **136**, 54–80 (2017).

53.   Mahapatra, A. *et al.* A review of aspects of additive engineering in perovskite solar cells. *J Mater Chem A Mater* **8**, 27–54 (2020).

54.   Yin, X., Song, Z., Li, Z. & Tang, W. Toward ideal hole transport materials: A review on recent progress in dopant-free hole transport materials for fabricating efficient and stable perovskite solar cells. *Energy Environ Sci* **13**, 4057–4086 (2020).

55.   Jung, E. H. *et al.* Efficient, stable and scalable perovskite solar cells using poly(3-hexylthiophene). *Nature* **567**, 511–515 (2019).

56.   Lee, H. K. H. *et al.* Outstanding Indoor Performance of Perovskite Photovoltaic Cells – Effect of Device Architectures and Interlayers. *Solar RRL* **3**, 1–7 (2019).

57.   Chiang, C. H. & Wu, C. G. Bulk heterojunction perovskite-PCBM solar cells with high fill factor. *Nat Photonics* **10**, 196–200 (2016).

58.   Park, H., Chaurasiya, R., Jeong, B. H., Sakthivel, P. & Park, H. J. Nickel Oxide for Perovskite Photovoltaic Cells. *Adv Photonics Res* **2**, 2000178 (2021).

59.   Zuo, C. & Ding, L. Solution-Processed Cu2O and CuO as Hole Transport Materials for Efficient Perovskite Solar Cells. *Small* **11**, 5528–5532 (2015).

60.   Mora-Seró, I. How Do Perovskite Solar Cells Work? *Joule* **2**, 585–587 (2018).

61.   Kirchartz, T., Bisquert, J., Mora-Sero, I. & Garcia-Belmonte, G. Classification of solar cells according to mechanisms of charge separation and charge collection. *Physical Chemistry Chemical Physics* **17**, 4007–4014 (2015).

62.   Stolterfoht, M. *et al.* The impact of energy alignment and interfacial recombination on the internal and external open-circuit voltage of perovskite solar cells. *Energy Environ Sci* **12**, 2778–2788 (2019).

63.   De Wolf, S. *et al.* Organometallic halide perovskites: Sharp optical absorption edge and its relation to photovoltaic performance. *Journal of Physical Chemistry Letters* **5**, 1035–1039 (2014).

64.   Elumalai, N. K., Mahmud, M. A., Wang, D. & Uddin, A. Perovskite solar cells: Progress and advancements. *Energies (Basel)* **9**, (2016).

65.   Stoumpos, C. C. & Kanatzidis, M. G. The Renaissance of Halide Perovskites and Their Evolution as Emerging Semiconductors. *Acc Chem Res* **48**, 2791–2802 (2015).

66.   Wang, S. *et al.* Chlorine retention enables the indoor light harvesting of triple halide wide bandgap perovskites. *J Mater Chem A Mater* **11**, 12328–12341 (2023).

67.   Xu, J. *et al.* Triple-halide wide-band gap perovskites with suppressed phase segregation for efficient tandems. *Science (1979)* **367**, 1097–1104 (2020).

68.   Leijtens, T., Bush, K. A., Prasanna, R. & McGehee, M. D. Opportunities and challenges for tandem solar cells using metal halide perovskite semiconductors. *Nat Energy* **3**, 828–838 (2018).

69. Tong, J. *et al.* Carrier lifetimes of >1 ms in Sn-Pb perovskites enable efficient all-perovskite tandem solar cells. *Science (1979)* **364**, 475–479 (2019).

70. Walsh, A. Principles of chemical bonding and band gap engineering in hybrid organic-inorganic halide perovskites. *Journal of Physical Chemistry C* **119**, 5755–5760 (2015).

71. Herz, L. M. Charge-Carrier Dynamics in Organic-Inorganic Metal Halide Perovskites. *Annu Rev Phys Chem* **67**, 65–89 (2016).

72. Li, M., Fu, J., Xu, Q. & Sum, T. C. Slow Hot-Carrier Cooling in Halide Perovskites: Prospects for Hot-Carrier Solar Cells. *Advanced Materials* vol. 31 Preprint at https://doi.org/10.1002/adma.201802486 (2019).

73. Stranks, S. D. & Petrozza, A. Revisiting photocarrier lifetimes in photovoltaics. *Nature Photonics* vol. 10 562 Preprint at https://doi.org/10.1038/nphoton.2016.164 (2016).

74. Dequilettes, D. W. *et al.* Charge-Carrier Recombination in Halide Perovskites. *Chemical Reviews* vol. 119 11007–11019 Preprint at https://doi.org/10.1021/acs.chemrev.9b00169 (2019).

75. Xia, J., Sohail, M. & Nazeeruddin, M. K. Efficient and Stable Perovskite Solar Cells by Tailoring of Interfaces. *Advanced Materials* vol. 35 Preprint at https://doi.org/10.1002/adma.202211324 (2023).

76. Dequilettes, D. W. *et al.* Charge-Carrier Recombination in Halide Perovskites. *Chemical Reviews* vol. 119 11007–11019 Preprint at https://doi.org/10.1021/acs.chemrev.9b00169 (2019).

77. Simbula, A. *et al.* Direct measurement of radiative decay rates in metal halide perovskites†. *Energy Environ Sci* **15**, 1211–1221 (2022).

78. Stranks, S. D. Nonradiative Losses in Metal Halide Perovskites. *ACS Energy Letters* vol. 2 1515–1525 Preprint at https://doi.org/10.1021/acsenergylett.7b00239 (2017).

79. de Quilettes, D. W. *et al.* Impact of microstructure on local carrier lifetime in perovskite solar cells. *Science (1979)* **348**, 683–686 (2015).

80. Manser, J. S., Christians, J. A. & Kamat, P. V. Intriguing Optoelectronic Properties of Metal Halide Perovskites. *Chemical Reviews* vol. 116 12956–13008 Preprint at https://doi.org/10.1021/acs.chemrev.6b00136 (2016).

81. Stranks, S. D. *et al.* Recombination Kinetics in Organic-Inorganic Perovskites: Excitons, Free Charge, and Subgap States. *Phys Rev Appl* **2**, (2014).

82. Kang, J. & Wang, L. W. High Defect Tolerance in Lead Halide Perovskite CsPbBr3. *Journal of Physical Chemistry Letters* **8**, 489–493 (2017).

83. Walsh, A. & Zunger, A. *Instilling Defect Tolerance in New Compounds*. *Nature Publishing Group* www.nature.com/naturematerials (2017) doi:10.1038/nmat.4973.

84. Steirer, K. X. *et al.* Defect Tolerance in Methylammonium Lead Triiodide Perovskite. *ACS Energy Lett* **1**, 360–366 (2016).

85. Steirer, K. X. *et al.* Defect Tolerance in Methylammonium Lead Triiodide Perovskite. *ACS Energy Lett* **1**, 360–366 (2016).

86. Kim, J. *et al.* Excitation Density Dependent Photoluminescence Quenching and Charge Transfer Efficiencies in Hybrid Perovskite/Organic Semiconductor Bilayers. *Adv Energy Mater* **8**, (2018).

87. Abdi-Jalebi, M. *et al.* Maximizing and stabilizing luminescence from halide perovskites with potassium passivation. *Nature* **555**, 497–501 (2018).

88. Fan, L. *et al.* Elucidating the role of chlorine in perovskite solar cells. 7423–7432 (2017) doi:10.1039/c7ta00973a.

89. Garai, R., Gupta, R. K. & Iyer, P. K. Trap State Passivation for Stabilizing Perovskite Solar Cells via Multifunctional Molecules. *Accounts of Materials Research* vol. 4 560–565 Preprint at https://doi.org/10.1021/accountsmr.2c00207 (2023).

90. Min, H. *et al.* Perovskite solar cells with atomically coherent interlayers on SnO2 electrodes. *Nature* **598**, 444–450 (2021).

91. Wolff, C. M., Caprioglio, P., Stolterfoht, M. & Neher, D. Nonradiative Recombination in Perovskite Solar Cells: The Role of Interfaces. *Advanced Materials* **31**, (2019).

92. Kim, G. *et al.* Transparent Thin-Film Silicon Solar Cells for Indoor Light Harvesting with Conversion Efficiencies of 36% without Photodegradation. *ACS Appl Mater Interfaces* **12**, 27122–27130 (2020).

93. Wang, Z. *et al.* Organic photovoltaic cells offer ultrahigh VOC of ∼ 1.2 V under AM 1.5G light and a high efficiency of 21.2 % under indoor light. *Chemical Engineering Journal* **451**, 139080 (2023).

94. Zhang, D. *et al.* A molecular photosensitizer achieves a V oc of 1.24 V enabling highly efficient and stable dye-sensitized solar cells with copper(II/I)-based electrolyte. *Nat Commun* **12**, 2–11 (2021).

95. Teran, A. S. *et al.* AlGaAs Photovoltaics for Indoor Energy Harvesting in mm-Scale Wireless Sensor Nodes. *IEEE Trans Electron Devices* **62**, 2170–2175 (2015).

96. Guo, Z., Jena, A. K. & Miyasaka, T. Halide Perovskites for Indoor Photovoltaics: The Next Possibility. *ACS Energy Lett* 90–95 (2022) doi:10.1021/acsenergylett.2c02268.

97. Muhammad, B. T., Kar, S., Stephen, M. & Leong, W. L. Halide perovskite-based indoor photovoltaics: recent development and challenges. *Mater Today Energy* **23**, 100907 (2022).

98. De Rossi, F., Pontecorvo, T. & Brown, T. M. Characterization of photovoltaic devices for indoor light harvesting and customization of flexible dye solar cells to deliver superior efficiency under artificial lighting. *Appl Energy* **156**, 413–422 (2015).

99. Pecunia, V., Occhipinti, L. G. & Hoye, R. L. Z. Emerging Indoor Photovoltaic Technologies for Sustainable Internet of Things. *Adv Energy Mater* (2021) doi:10.1002/aenm.202100698.

100. Lee, C., Lee, J. H., Lee, H. H., Nam, M. & Ko, D. H. Over 30% Efficient Indoor Organic Photovoltaics Enabled by Morphological Modification Using Two Compatible Non-Fullerene Acceptors. *Adv Energy Mater* **12**, 1–10 (2022).

101. Kim, J. *et al.* Revisiting the Classical Wide-Bandgap HOMO and Random Copolymers for Indoor Artificial Light Photovoltaics. *Macromol Rapid Commun* **43**, 1–11 (2022).

102. Saeed, M. A. *et al.* 2D MXene Additive-Induced Treatment Enabling High-Efficiency Indoor Organic Photovoltaics. *Adv Opt Mater* **11**, 1–11 (2023).

103. Hyuk Kim, T., Jin Chung, J., Ahsan Saeed, M., Youn Lee, S. & Won Shim, J. High-efficiency (over 33 %) indoor organic photovoltaics with band-aligned and defect-suppressed interlayers. *Appl Surf Sci* **610**, 155558 (2023).

104. Chen, C. *et al.* Anthracene-Bridged Sensitizers for Dye-Sensitized Solar Cells with 37% Efficiency under Dim Light (Adv. Energy Mater. 20/2022). *Adv Energy Mater* **12**, 2270080 (2022).

105. Mozaffari, S., Nateghi, M. R. & Zarandi, M. B. An overview of the Challenges in the commercialization of dye sensitized solar cells. *Renewable and Sustainable Energy Reviews* **71**, 675–686 (2017).

106. Shin, S. C. *et al.* Ultra-thick semi-crystalline photoactive donor polymer for efficient indoor organic photovoltaics. *Nano Energy* **58**, 466–475 (2019).

107. Di Giacomo, F. *et al.* Mesoporous perovskite solar cells and the role of nanoscale compact layers for remarkable all-round high efficiency under both indoor and outdoor illumination. *Nano Energy* **30**, 460–469 (2016).

108. Lucarelli, G., Giacomo, F. Di, Zardetto, V., Creatore, M. & Brown, T. M. Efficient light harvesting from flexible perovskite solar cells under indoor white light-emitting diode illumination. *Nano Research 2016 10:6* **10**, 2130–2145 (2017).

109. Dagar, J., Castro-Hermosa, S., Lucarelli, G., Cacialli, F. & Brown, T. M. Highly efficient perovskite solar cells for light harvesting under indoor illumination via solution processed SnO2/MgO composite electron transport layers. *Nano Energy* **49**, 290–299 (2018).

110. Jagadamma, L. K., Blaszczyk, O., Sajjad, M. T., Ruseckas, A. & Samuel, I. D. W. Efficient indoor p-i-n hybrid perovskite solar cells using low temperature solution processed NiO as hole extraction layers. *Solar Energy Materials and Solar Cells* **201**, 110071 (2019).

111. Sun, H. *et al.* Realizing Stable Artificial Photon Energy Harvesting Based on Perovskite Solar Cells for Diverse Applications. *Small* **16**, 1–9 (2020).

112. Hoke, E. T. *et al.* Reversible photo-induced trap formation in mixed-halide hybrid perovskites for photovoltaics. *Chem Sci* **6**, 613–617 (2015).

113. Xu, J. *et al.* Triple-halide wide-band gap perovskites with suppressed phase segregation for efficient tandems. *Science (1979)* **367**, 1097–1104 (2020).

114. Kim, J. *et al.* Chlorine Incorporation in Perovskite Solar Cells for Indoor Light Applications. *Cell Rep Phys Sci* **1**, 100273 (2020).

115. Jiang, Q. *et al.* Surface passivation of perovskite film for efficient solar cells. *Nat Photonics* **13**, 460–466 (2019).

116. Maqsood, A. *et al.* Organic Halide PEACl for Surface Passivation and Defects Suppression in Perovskite Solar Cells. *ACS Appl Energy Mater* **4**, 12411–12420 (2021).

117. Zhang, S. *et al.* Grain Boundary and Buried Interface Suturing Enabled by Fullerene Derivatives for High-Performance Perovskite Solar Module. *ACS Energy Lett* **7**, 3958–3966 (2022).

118. Al-Ashouri, A. *et al.* Conformal monolayer contacts with lossless interfaces for perovskite single junction and monolithic tandem solar cells. *Energy Environ Sci* **12**, 3356–3369 (2019).

119. Yang, M. *et al.* Reducing lead toxicity of perovskite solar cells with a built-in supramolecular complex. *Nat Sustain* **6**, (2023).

120. Li, X. *et al.* Strain Regulation of Mixed-Halide Perovskites Enables High-Performance Wide-Bandgap Photovoltaics. *Advanced Materials* (2024) doi:10.1002/adma.202401103.

121. Li, M. *et al.* Interface Modification by Ionic Liquid: A Promising Candidate for Indoor Light Harvesting and Stability Improvement of Planar Perovskite Solar Cells. *Adv Energy Mater* **8**, 1–8 (2018).

122. Jiang, B. *et al.* Enhancing the Efficiency of Indoor Perovskite Solar Cells through Surface Defect Passivation with Coplanar Heteroacene Cored A–D–A-type Molecules. *Adv Funct Mater* (2023) doi:10.1002/adfm.202312819.

123. Skafi, Z. *et al.* Highly Efficient Flexible Perovskite Solar Cells on Polyethylene Terephthalate Films via Dual Halide and Low-Dimensional Interface Engineering for Indoor Photovoltaics. *Solar RRL* **7**, 1–9 (2023).

124. Li, Y. *et al.* In Situ Formation of 2D Perovskite Seeding for Record-Efficiency Indoor Perovskite Photovoltaic Devices. *Advanced Materials* **2306870**, 1–10 (2023).

125. Han, E. Q. *et al.* High-Performance Indoor Perovskite Solar Cells by Self-Suppression of Intrinsic Defects via a Facile Solvent-Engineering Strategy. *Small* (2023) doi:10.1002/smll.202305192.

126. He, X. *et al.* 40.1% Record Low-Light Solar-Cell Efficiency by Holistic Trap-Passivation using Micrometer-Thick Perovskite Film. *Advanced Materials* **2100770**, 1–10 (2021).

127. Ma, Q. *et al.* One-step dual-additive passivated wide-bandgap perovskites to realize 44.72%-efficient indoor photovoltaics. *Energy Environ Sci* **17**, 1637–1644 (2024).

128. Barbosa-García, O. *et al.* UV-vis absorption spectroscopy and multivariate analysis as a method to discriminate tequila. *Spectrochim Acta A Mol Biomol Spectrosc* **66**, 129–134 (2007).

129. Rocha, F. S., Gomes, A. J., Lunardi, C. N., Kaliaguine, S. & Patience, G. S. Experimental methods in chemical engineering: Ultraviolet visible spectroscopy—UV-Vis. *Canadian Journal of Chemical Engineering* **96**, 2512–2517 (2018).

130. Baikie, I. D., Grain, A. C., Sutherland, J. & Law, J. Ambient pressure photoemission spectroscopy of metal surfaces. in *Applied Surface Science* vol. 323 45–53 (Elsevier B.V., 2014).

131. Fowler, R. H. The Analysis of Photoelectric Sensitivity Curves for Clean Metals at Various Temperatures. *Physical Review* **38**, 45–56 (1931).

132. Halder, A. & Kresin, V. V. Nanocluster ionization energies and work function of aluminum, and their temperature dependence. *Journal of Chemical Physics* **143**, (2015).

133. Qin, M., Chan, P. F. & Lu, X. A Systematic Review of Metal Halide Perovskite Crystallization and Film Formation Mechanism Unveiled by In Situ GIWAXS. *Advanced Materials* vol. 33 Preprint at https://doi.org/10.1002/adma.202105290 (2021).

134. Vegso, K. *et al.* Kinetics of Polymer-Fullerene Phase Separation during Solvent Annealing Studied by Table-Top X-ray Scattering. *ACS Appl Mater Interfaces* **9**, 8241–8247 (2017).

135. Schlipf, J. & Müller-Buschbaum, P. Structure of Organometal Halide Perovskite Films as Determined with Grazing-Incidence X-Ray Scattering Methods. *Adv Energy Mater* **7**, (2017).

136. Baker, J. L. *et al.* Quantification of thin film cristallographic orientation using X-ray diffraction with an area detector. *Langmuir* **26**, 9146–9151 (2010).

137. Brown, P. E. *et al.* Distinguishing Electron Diffusion and Extraction in Methylammonium Lead Iodide. *Journal of Physical Chemistry Letters* **14**, 3007–3013 (2023).

138. Krogmeier, B., Staub, F., Grabowski, D., Rau, U. & Kirchartz, T. Quantitative analysis of the transient photoluminescence of CH 3 NH 3 PbI 3 /PC 61 BM heterojunctions by numerical simulations. *Sustain Energy Fuels* **2**, 1027–1034 (2018).

139. Edwards, P. R. *et al.* High-resolution cathodoluminescence hyperspectral imaging of nitride nanostructures. in *Microscopy and Microanalysis* vol. 18 1212–1219 (2012).

140. Guthrey, H. & Moseley, J. A Review and Perspective on Cathodoluminescence Analysis of Halide Perovskites. *Advanced Energy Materials* vol. 10 Preprint at https://doi.org/10.1002/aenm.201903840 (2020).

141. Ryan, J. W. & Palomares, E. Photo-Induced Charge Carrier Recombination Kinetics in Small Molecule Organic Solar Cells and the Influence of Film Nanomorphology. *Advanced Energy Materials* vol. 7 Preprint at https://doi.org/10.1002/aenm.201601509 (2017).

142. Singh, S. & Kabra, D. Comparative Study of Recombination Dynamics in Optimized Composition of Sn- Versus Pb-Based Perovskite Solar Cells. *ACS Appl Mater Interfaces* **13**, 42297–42306 (2021).

143. Duijnstee, E. A. *et al.* Toward Understanding Space-Charge Limited Current Measurements on Metal Halide Perovskites. *ACS Energy Lett* **5**, 376–384 (2020).

144. Le Corre, V. M. *et al.* Revealing Charge Carrier Mobility and Defect Densities in Metal Halide Perovskites via Space-Charge-Limited Current Measurements. *ACS Energy Lett* **6**, 1087–1094 (2021).

145. Ollearo, R. *et al.* Ultralow dark current in near-infrared perovskite photodiodes by reducing charge injection and interfacial charge generation. *Nat Commun* **12**, (2021).

146. Zhang, D. D., Wei, H. X. & Zhu, L. Q. Suppressing dark current for high-detectivity perovskite photodetectors via defect passivation. *Org Electron* **114**, (2023).

147. Lin, R. *et al.* All-perovskite tandem solar cells with 3D/3D bilayer perovskite heterojunction. *Nature* **620**, 994–1000 (2023).

148.   Jiang, Q. *et al.* Towards linking lab and field lifetimes of perovskite solar cells. *Nature* **623**, 313–318 (2023).

149.   Ye, F. *et al.* Overcoming C60-induced interfacial recombination in inverted perovskite solar cells by electron-transporting carborane. *Nat Commun* **13**, (2022).

150.   Wang, Y. *et al.* Oxidation-resistant all-perovskite tandem solar cells in substrate configuration. *Nat Commun* **14**, (2023).

151.   Li, C. *et al.* Highly Visible-Transparent and Color-Neutral Perovskite Solar Cells for Self-Powered Smart Windows. *Solar RRL* **6**, (2022).

152.   Zia, W. *et al.* MAPbCl3 Light Absorber for Highest Voltage Perovskite Solar Cells. *ACS Energy Lett* **9**, 1017–1024 (2024).